Chapter 12

Atomistic Simulations of the Generation of Nanoparticles in Short-Pulse Laser Ablation of Metals: Effect of Background Gas and Liquid Environments

Cheng-Yu Shih,[a] Chengping Wu,[a] Han Wu,[a,b,c] Maxim V. Shugaev,[a] and Leonid V. Zhigilei[a]

[a]*Department of Materials Science and Engineering, University of Virginia, 395 McCormick Road, Charlottesville, VA 22904-4745, USA*

[b]*Institute of Modern Optics, Nankai University, 94 Weijin Road, Tianjin 300071, China*

[c]*School of Mechanical Science and Engineering, Huazhong University of Science and Technology, 1037 Luoyu Road, Wuhan, 430074, China*

lz2n@virginia.edu

Atomistic simulations are playing an increasingly important role in the investigation of the fundamental mechanisms of laser-material interactions. The advancements in the computational methodology and fast growth of available computing resources are rapidly expanding the range of problems amenable to atomistic modeling. This chapter provides an overview of the results obtained in recent simulations of laser ablation of metal targets in vacuum, a background gas, and a liquid environment. A comparison of the

Pulsed Laser Ablation: Advances and Applications in Nanoparticles and Nanostructuring Thin Films
Edited by Ion N. Mihailescu and Anna Paola Caricato

ISBN 978-981-4774-23-9 (Hardcover), 978-1-315-18523-1 (eBook)
www.panstanford.com

results of the simulations of laser ablation of Al targets in vacuum and in a 1 atm Ar background gas reveals a surprisingly strong effect of the gas environment on the initial plume dynamics and the cluster size distribution, with almost complete suppression of the generation of small atomic clusters in the front part of the ablation plume. A stronger spatial confinement of laser ablation by a liquid environment, investigated for Ag targets in water, is found to suppress the material ejection and produce large frozen subsurface voids at low laser fluences and a dense layer of superheated liquid metal at the front of the ejected ablation plume at higher fluences. The implications of the computational predictions for interpretation of experimental data on the effect of background gas and liquid environments on the generation of nanoparticles in laser ablation are discussed.

12.1 Introduction

"Laser ablation" is a term used to describe material removal from a target irradiated by a laser pulse. A wide range of practical applications of laser ablation includes generation of chemically clean and environmentally friendly nanoparticles [1]. The production of nanoparticles through direct laser ablation of an irradiated target eliminates the need for chemical precursors and presents a number of important advantages over conventional multistep chemical synthesis methods that introduce contamination from intermediate reactants and/or produce agglomerated structures with degraded functionality. The size, shape, structure, and composition of nanoparticles generated by laser ablation can be controlled by changing the target structure and composition [2], varying the background gas environment [3, 4], or mixing ablation plumes generated by double-pulse irradiation [5, 6]. Short-pulse (fs-ps) laser sources are especially suitable for nanoparticle production due to more localized and intense laser heating compared to nanosecond laser pulses [7–10] that increase the fraction of nanoparticles in the ablation plume [11–14].

Laser ablation in a liquid environment has recently emerged as a particularly promising approach to the generation of colloidal solutions of contamination-free nanoparticles [1, 15–18]. The

characteristics of nanoparticles in this case are affected by the choice of the liquid medium [19–21], its temperature [22], and the presence of surfactants [23–27]. The highly nonequilibrium conditions created by the interaction of the ablation plume with a liquid environment can result in the formation of nanoparticles with unusual structures, shapes, and composition, such as nanocubes [28], hollow spheroids [29, 30], patch-joint football-like AgGe microspheres [31], and diamond nanocrystallites produced by the laser ablation of graphite [32].

The main obstacles to broadening the range of practical applications benefiting from nanoparticle synthesis by laser ablation are the relatively low productivity [33] and wide (and often bimodal) nanoparticle size distributions [34–36]. The latter can be related to the variability of the nanoparticle formation mechanisms in different parts of the ablation plume [37–40], as well as the generation of large micron-size droplets by hydrodynamic sputtering of the melted pool or rupturing of liquid layers separated/spalled from the target in the course of the relaxation of laser-induced pressure [38, 41, 42]. Further progress in the optimization of experimental parameters for the efficient generation of nanoparticles with a narrow size distribution, required for advanced sensing, catalysis, and biomedical applications, can be facilitated by improved physical understanding of the involved processes.

While the general mechanisms of laser melting, spallation, and ablation in vacuum have been extensively studied experimentally, theoretically, and computationally, the effect of spatial confinement by a high-pressure (1 atm or higher) background gas, a liquid environment, or a solid overlayer on the laser-induced processes still remains largely unexplored. Introduction of spatial confinement and the interaction between the ejected plume and the surrounding medium adds another layer of complexity to the description of short-pulse laser ablation, which by itself is a complex and highly nonequilibrium phenomenon. As a result, the theoretical analysis of the nanoparticle formation by laser ablation in liquids [43] is largely based on semiquantitative models that adopt the concepts developed for the plume expansion in a background gas to the much stronger confinement by a liquid environment, and describes the nanoparticle formation as a process of coalescence of clusters in a

supersaturated solution formed by the mixing of the ablation plume and the liquid. The analysis in this case relies on the assumptions of the initial cluster size distribution in the solution, the temperature evolution in the plume–liquid mixing region, the thickness of the mixing region, and other parameters. While the continuum-level modeling can provide additional insights into the ablation dynamics [44, 45], some of the key processes, such as the mixing of the ablation plume with a liquid environment and the generation of nanoparticles in the mixed region, cannot be easily included in the continuum models.

Under conditions when the analytical and continuum-level numerical descriptions of spatially confined laser ablation are hindered by the complexity and highly nonequilibrium nature of laser-induced processes, the molecular dynamics (MD) computer simulation technique can serve as a useful alternative approach, capable of providing atomic-level insights into the laser-induced processes. The main advantage of the MD technique is that no assumptions are made on the processes or mechanisms under study. The only input in the MD model is the interatomic interaction potential that defines the equilibrium structure and thermodynamic properties of the material. The interatomic potentials are typically designed via ab initio calculations and fitted to reproduce basic material properties of interests. Once the interatomic potential is chosen and initial conditions are defined, the MD trajectories (positions and velocities) are obtained through numerical solution of the equations of motion for all atoms in the system without any further assumptions. This advantage makes MD an ideal technique for exploring nonequilibrium processes and revealing new physical phenomena.

Indeed, over the last 20 years MD simulations have been actively used in investigations of laser-induced generation of crystal defects, melting, and resolidification [46–57], as well as photomechanical spallation [38, 42, 55, 58–61] and ablation of various material systems [35, 37, 38, 55, 59, 60, 62–82]. Some of the results of MD simulation of laser-material interaction have been reviewed in Refs. [83–85]. Most of the MD simulations of laser ablation, however, have been performed for vacuum conditions, with the exception of a series of simulations of shock wave formation in laser ablation of an argon target in a background gas [77–80] and a

two-dimensional simulation of laser ablation of a target covered by a thin (400 monolayers thick) wetting layer [86]. The focus of the simulations reported in Refs. [77–80] was on the characteristics of the shock waves produced by the interaction of the ablation plume with the surrounding gas, and the effect of the background gas on the generation of clusters and nanoparticles was not analyzed. The qualitative conclusion of Ref. [86] on the decrease of the size of the ejected clusters in the presence of a wetting layer has to be verified and quantified in more realistic three-dimensional simulations.

In this chapter, we provide an overview of the results obtained in recent MD simulations of laser ablation of metal targets in vacuum, a high-pressure background gas, and a liquid environment. The computational methodology developed for MD simulations of laser interactions with metal targets is briefly discussed in Section 12.2, with a particular focus on a computationally efficient description of the ablation plume interaction with the background gas and liquid environment. A brief overview of the relatively well-established mechanisms of laser ablation in vacuum is provided and illustrated by the results of recent large-scale MD simulations in Section 12.3. The effect of the background gas on the dynamics of the ablation plume and nanoparticle size distribution is discussed in Section 12.4. The results of the first MD simulations of laser ablation in water are described in Section 12.5. The overall conclusions on the effect of the background gas and liquid environment on the mechanisms of nanoparticle generation are provided in Section 12.6.

12.2 Computational Setup for the Simulation of Laser Interactions with Metals in a Background Gas or Liquid Environment

The simulations discussed in this chapter are performed with a hybrid computational model combining the classical MD method with a continuum-level description of the laser excitation and subsequent relaxation of the conduction band electrons. The basic concepts of the model as well as the new computational developments enabling the simulations of laser ablation in a background gas and in liquids are briefly described below.

12.2.1 Representation of Laser Interaction with Metals

Although the MD method is capable of providing detailed information on the microscopic mechanisms of laser ablation, several modifications have to be made in order to apply the classical MD for simulations of laser interactions with metals. In particular, a realistic description of the laser coupling to the target material, the kinetics of thermalization of the absorbed laser energy, and the fast electron heat conduction should be incorporated into the MD technique. These processes can be accounted for by incorporating the MD method into the general framework of the two-temperature model (TTM) [87, 88] commonly used in the simulations of short-pulse laser interactions with metals. The idea of the combined TTM-MD model [38, 48, 55] is schematically illustrated in Fig. 12.1 and is briefly explained below.

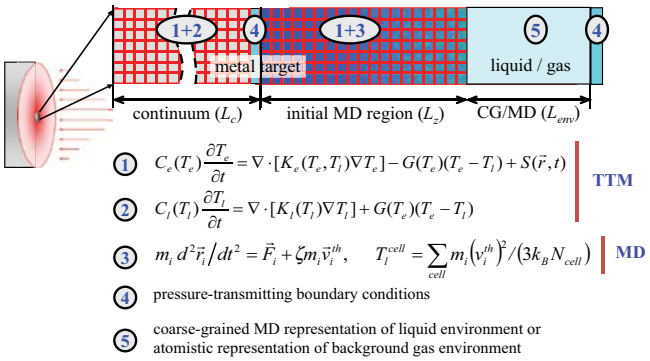

Figure 12.1 Schematic representation of the combined continuum–coarse-grained–atomistic model for the simulation of laser interactions with metals in a background gas or liquid environment. The metal target is represented by the TTM-MD model [38, 48], the liquid environment is simulated with a coarse-grained model [105], described in Section 12.2.2, and the simulations in a background gas are performed in the presence of a large gas-phase region equilibrated at the desired temperature and pressure. The spatial discretization in the continuum part of the model and the dimensions of the atomistic and continuum regions are not drawn to scale.

In the original TTM, the time evolution of the lattice and electron temperatures, T_l and T_e, is described by two coupled differential equations (Eqs. 12.1 and 12.2 in Fig. 12.1) that account for the electron heat conduction in the metal target and the energy

exchange between the electrons and atomic vibrations. In the combined TTM-MD method, MD substitutes the TTM equation for the lattice temperature in the surface region of the target, where laser-induced structural and phase transformations take place. The diffusion equation for the electron temperature, T_e, is solved by a finite difference method simultaneously with MD integration of the equations of motion of atoms. The cells in the finite difference discretization are related to the corresponding volumes of the MD system, and the local lattice temperature, T_l^{cell}, is defined for each cell from the average kinetic energy of the thermal motion of atoms. The electron temperature enters a coupling term, $\xi m_i \vec{v}_i^{th}$, that is added to the MD equations of motion to account for the energy exchange between the electrons and atomic vibrations. In this coupling term, ξ is a coefficient that depends on the instantaneous difference between the local lattice and electron temperatures as well as the strength of the electron–phonon coupling [48], m_i is the mass of an atom *i*, $\vec{v}_i^{th}$ is the thermal velocity of the atom defined as $\vec{v}_i^{th} = \vec{v}_i - \vec{v}^c$, where $\vec{v}_i$ is the actual velocity of atom *i* and $\vec{v}^c$ is the velocity of the center of mass of a cell to which atom *i* belongs. The expansion, density variation, and at higher fluences, disintegration of the irradiated target predicted in the MD part of the model are accounted for through the corresponding changes of the parameters of the TTM equation for electron temperature. The three-dimensional solution of the diffusion equation for T_e is used in simulations of laser spallation and ablation [38, 56, 61], where the dynamic material decomposition may result in lateral density and temperature variations.

In the continuum part of the model, beyond the surface region represented by the MD method, the electron heat conduction and the energy exchange between the electrons and the lattice are described by the conventional TTM equations, with L_c = 2–6 μm chosen to ensure negligible temperature changes at the bottom of the computational domain during the simulation time. A dynamic pressure-transmitting boundary condition [89–92] is applied at the bottom of the MD part of the system (marked as ④ in Fig. 12.1) to ensure nonreflecting propagation of the laser-induced stress wave from the MD region of the computational system to the bulk of the target. The energy carried away by the stress wave is monitored,

allowing for control over the total energy conservation in the combined model [91].

In the simulations of laser interactions with thin films deposited on a substrate [35], the atomistic TTM-MD representation is extended to the whole metal film, with a thickness L_z, and the boundary condition marked as ④ in the left part of Fig. 12.1 is modified to reproduce the elastic response of the substrate to the laser-induced pressure waves and the adhesion between the metal film and the substrate [35, 92]. The acoustic impedance matching boundary condition at the substrate-film interface is parametrized in this case to ensure the partial reflection of the laser-induced pressure wave from the interface, as well as the work of adhesion between the silica substrate and metal film. In an alternative method for the description of the metal-substrate interface, a part of the substrate is represented with atomic resolution [92], thus accounting not only for the elastic response of the substrate but also for the possibility of plastic deformation, melting, and atomic mixing in the region of the substrate adjacent to the metal film.

The choice of the interatomic potential in MD simulations defines all the thermal and elastic properties of the target material, such as the lattice heat capacity, elastic moduli, coefficient of thermal expansion, melting temperature, volume, and enthalpy of melting and vaporization. In the simulations discussed in this chapter, the interatomic interactions are described by the embedded atom method (EAM) potentials [93] that provide a computationally efficient but still realistic description of bonding in metals. In particular, an EAM potential for Al developed by Mishin et al. [94, 95] is used in the simulations discussed in Sections 12.3 and 12.4, and an EAM potential for Ag designed by Foiles, Baskes, and Daw [96] is used in Section 12.5.

The electron temperature dependences of the thermophysical material properties included in the TTM equation for the electron temperature (electron–phonon coupling factor G, the electron heat capacity C_e, and the heat conductivity K_e; see Fig. 12.1) are highly sensitive to details of the electronic structure of the material and can exhibit large deviations (up to an order of magnitude) from the commonly used approximations of a linear temperature dependence of the electron heat capacity and a constant electron–phonon coupling [97–99]. These deviations have important implications

for quantitative computational analysis of ultrafast processes associated with fs laser interaction with metals [52–54, 97, 98] and are accounted for in the TTM-MD model.

12.2.2 Representation of Background Gas and Liquid Environments

The background gas environment is introduced into the model in a rather straightforward manner, by simply adding a region with gas-phase molecules/atoms equilibrated at the desired temperature and pressure above the surface of the target, as shown in Fig. 12.1. The size of the region, L_{env} in Fig. 12.1, is chosen to be sufficiently large to ensure that the shock wave generated in the background gas by the ejection of the ablation plume would not reach the upper end of the region during the time of the simulation. A simple rigid plane is used in this case as the upper boundary of the background gas region instead of the pressure-transmitting boundary shown in Fig. 12.1. This brute force approach is possible because the computational overhead added by the treatment of the background gas is relatively small. For example, in the simulations of laser ablation of Al targets discussed in Section 12.4, an Ar gas region with L_{env} = 4 μm contributes only 0.5 to 5% of the total number of atoms for the values of the background gas pressure ranging from 1 to 10 atm.

The interatomic interactions between Ar and Al atoms are described by the Lennard–Jones (LJ) potential, with the parameters for Ar-Ar adopted from Ref. [100] and the ones for Ar-Al fitted to the results of ab initio calculations of the adsorption energy of an Ar on Al (111) surface [101]. At short distances (high interaction energies), the LJ potential for Ar-Al interactions is substituted by the Ziegler–Biersack–Littmark (ZBL) potential [102], which provides a more realistic description of the energetic collisions between the Al and Ar atoms at the initial stage of the plume expansion. The LJ and ZBL potentials are smoothly connected with each other by a second-order polynomial applied in the range of distances that correspond to the energy of the repulsive interaction ranging from –0.026 to 0.220 eV.

The computational description of the liquid environment presents a bigger computational challenge as compared to that of the background gas. The direct application of the conventional

all-atom MD representation of liquids in large-scale simulations of laser processing or ablation is not feasible due to the high computational cost. Thus, a coarse-grained representation of the liquid environment [59, 70], where each particle represents several molecules, is adapted in the simulations described in Section 12.5. The coarse-graining reduces the number of degrees of freedom treated in the MD simulations and, as a result, significantly increases the time and length scales accessible for the simulations. At the same time, however, the smaller number of the dynamic degrees of freedom results in a severe underestimation of the heat capacity of the liquid. To resolve this problem, the degrees of freedom missing in the coarse-grained model are accounted for through a heat bath approach that associates an internal energy variable with each coarse-grained particle [103–106]. The energy exchange between the internal (implicit) and dynamic (explicit) degrees of freedom is controlled by the dynamic coupling between the translational degrees of freedom and the vibrational (breathing) mode associated with each particle (the particles are allowed to change their radii, or to "breathe" [70, 105]). The energy exchange is implemented through the addition of a damping or viscosity force to the breathing mode, which connects the breathing mode to the energy bath with a capacity chosen to reproduce the real heat capacity of the group of atoms represented by each coarse-grained particle [105, 106]. In effect, the breathing mode serves as a "gate" for accessing the energy stored in the molecular heat bath.

The first implementation of the coarse-grained model with the heat bath approach was recently developed for water and applied in simulations of laser interactions with the water-lysozyme system [105] and ablation of thin Ag films in a water environment [106]. While one cannot expect the coarse-grained model to provide an accurate representation of all the structural and thermodynamic properties of water, the key physical properties predicted by the model, such as density, speed of sound, bulk modulus, viscosity, surface energy, melting temperature, critical temperature, and critical density, are found to not deviate from the experimental values by more than 25% [105, 106]. In the simulations discussed in Section 12.5, the potential describing the interactions between Ag atoms and the coarse-grained particles is fitted to match the

diffusion of metal atoms and small clusters in water, predicted in atomistic simulations performed at different temperatures.

12.3 Large-Scale MD Simulations of Laser Ablation in Vacuum

The MD simulations are based on the solution of the equations of motion for all atoms included in the computational system and, as a result, are generally limited to the treatment of submicron regions of the irradiated targets containing fewer than a billion (10^9) atoms. With a typical laser spot of tens to hundreds of microns and an ablation depth of tens to hundreds of nanometers, the number of atoms in a computational system that would be needed for the direct MD simulation of processes occurring on the scale of the whole laser spot can easily exceed trillions and is clearly beyond the current capabilities of the MD technique. Under these circumstances, the MD computational cell is typically assumed to represent a local volume within the laser spot, and the material response to local laser energy deposition is investigated, as schematically shown in the left part of Fig. 12.1. The periodic boundary conditions in the lateral directions, parallel to the surface of the target, are used in this case to reproduce the interaction of atoms in the MD computational cell with the surrounding material.

The processes occurring at the scale of the whole laser spot can still be investigated by combining results of simulations performed at different laser fluences and mapping them to the different locations within the laser spot. This mosaic approach is illustrated in Fig. 12.2 for an Al target irradiated by a 100 fs pulse with a Gaussian spatial profile of the laser beam. The snapshots shown in the figure are from five TTM-MD simulations performed at different laser fluences. The computational systems used in these simulations have lateral dimensions of 94 × 94 nm^2 and the depth of the atomistic part of the computational cell (L_z in Fig. 12.1) ranging from 150 nm for the lowest fluence to 300 nm for the highest one (the corresponding number of atoms is between 77 to 159 millions). The snapshots from individual TTM-MD simulations are shown for the same time of 150 ps after the laser pulse and are aligned with locations within the laser spot that correspond to the values of local fluence used in the

simulations, as shown by the vertical and horizontal dashed lines in the lower part of Fig. 12.2.

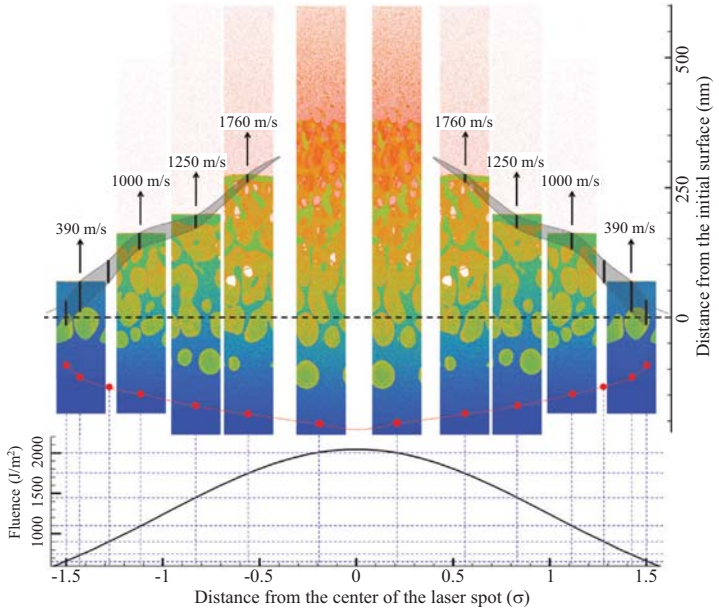

Figure 12.2 An illustration of the mosaic approach to the representation of the laser-induced processes at the scale of the whole laser spot, based on the results of a series of atomistic simulations performed for different laser fluences. The integral visual picture of melting, generation of subsurface voids, and material ejection is shown for an Al target irradiated by a 100 fs laser pulse. The laser beam has a Gaussian spatial profile with the standard deviation σ and a peak-absorbed laser fluence of 2050 J/m^2, as shown in the lower part of the figure. All snapshots are taken at the same time (150 ps) after the laser pulse and are aligned with locations within the laser spot that correspond to the values of the local fluence used in the simulations. The atoms in the snapshots are colored by their potential energy, from blue for low-energy atoms in the bulk of the target to red for the vapor-phase atoms. The red dots connected by the red line mark the location of the liquid–crystal interface. Reproduced from Ref. [38] with permission of Springer.

A mere visual inspection of Fig. 12.2 suggests coexistence of two distinct regimes of the material response to the laser energy deposition within the laser spot. In the periphery of the laser spot, a well-defined liquid layer can be seen at the top of the region of an expanding foamy structure of interconnected liquid regions. In

the central part of the laser spot, the top surface layer of the target undergoes an explosive decomposition into vapor and small liquid droplets. The transition between the two regimes is manifested by the disappearance of the top liquid layer and a sharp increase in the density of the vapor emitted from the irradiated surface.

The two distinct visual pictures of the ablation process can be related to the differences in the physical mechanisms driving the material ejection. In the periphery of the laser spot, the energy density is not sufficient enough to cause an explosive release of the vapor (so-called phase explosion or explosive boiling [37, 60, 107–109]), and the material ejection (commonly called "spallation" [41, 42]) is driven by the relaxation of laser-induced stresses. The photomechanical nature of the spallation is evident from Fig. 12.3a, where the evolution of pressure and temperature is shown for a sequence of consecutive 5 nm thick layers located at different depths in the initial target irradiated at an absorbed laser fluence of 1100 J/m^2. The initial increase in temperature and pressure in different layers (Fig. 12.3a) is related to the laser excitation and electron–phonon energy transfer taking place under conditions of stress confinement [55, 42], when the heating rate exceeds the rate of the mechanical equilibration (expansion) of the material. The degree of stress confinement is different in different layers, with the top layers starting to expand before the electron–phonon equilibration is completed, thus reducing the maximum pressure reached in these layers. The relaxation of the compressive pressure in the presence of the free surface results in the development of an unloading (tensile) component of the stress wave propagating from the irradiated surface to the bulk of the target. The strength of the unloading component of the wave increases with depth down to the layer located between 110 and 115 nm. The temperature–pressure trajectories for layers located between 15 and 80 nm cross the red line, marking the limit of the stability of the metastable liquid against the onset of the cavitation (determined in a series of constant-pressure MD simulations [38]) (Fig. 12.3b). The observation that the void formation is only observed in a region that corresponds to the layers that cross the red line supports the notion of the photomechanical nature of the driving forces responsible for the nucleation, growth, and coalescence of subsurface voids, which eventually lead to the ejection of liquid droplets in the spallation regime.

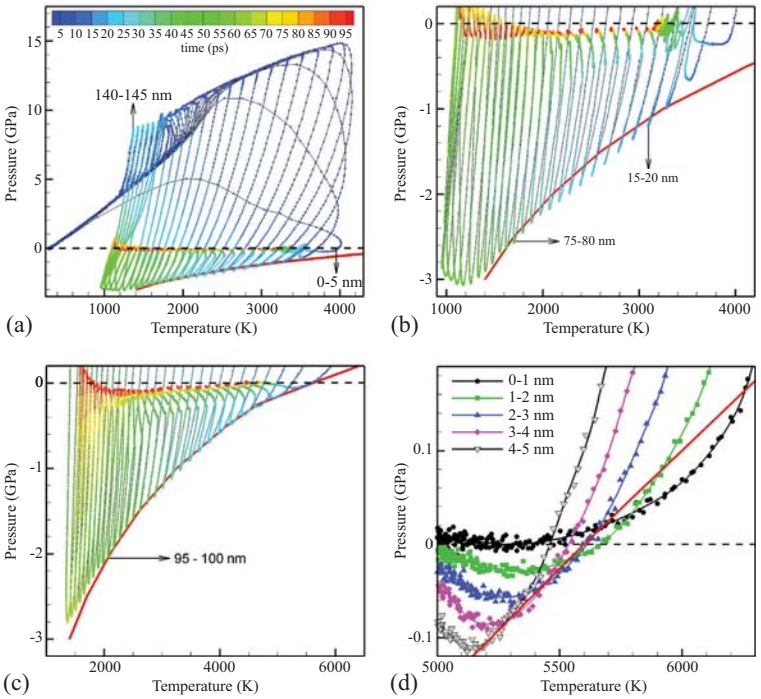

Figure 12.3 The evolution of temperature and pressure averaged over 5 nm thick (a–c) and 1 nm thick (d) consecutive layers located at different depths in the initial Al targets irradiated by 100 fs laser pulses at absorbed fluences of 1100 J/m^2 (a, b) and 2000 J/m^2 (c, d). The red line shows the temperature and pressure conditions for the onset of cavitation or phase explosion in the metastable liquid, calculated for Al represented by the EAM potential. Reproduced from Ref. [38] with permission of Springer.

In the central part of the laser spot, the temperature–pressure trajectories are similar to the ones discussed above, except that the higher energy density deposited in the top layers of the target makes the trajectories for the top layers cross the red line at higher temperatures and lower magnitudes of negative pressure, and even at positive pressure, as is the case for the three top 1 nm thick layers in Fig. 12.3c. The material decomposition in this case proceeds through the rapid (explosive) decomposition of the superheated liquid into vapor and small liquid droplets, signifying the transition to the phase explosion regime of laser ablation [55, 110]. Deeper

into the target, the propagation of the tensile component of the stress wave leads to the additional cavitation in the superheated liquid, with the density of vapor in the pores decreasing with depth, as can be seen from the series of snapshots shown in Fig. 12.4 for a simulation performed at a fluence of 2000 J/m^2. The pressure–temperature trajectories for the material initially located down to ~100 nm below the surface cross the red line that defines the limit of the stability of the metastable liquid against the onset of the cavitation at large negative stresses, suggesting that the relaxation of the tensile stresses rather than the release of vapor-phase atoms is providing the main driving force for the nucleation and growth of voids in this region. Hence, the dominant driving force responsible for the material decomposition changes with depth and contributes to the effect of spatial segregation of droplets that is commonly observed in the ablation plume.

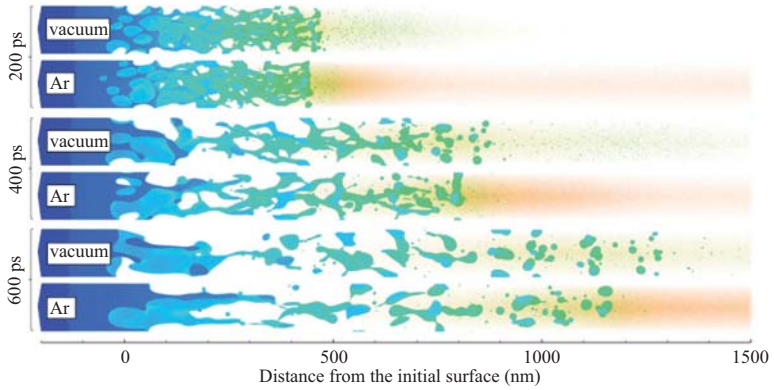

Figure 12.4 Snapshots of atomic configurations predicted in the TTM-MD simulation of laser ablation of a bulk Al target irradiated by a 100 fs laser pulse at an absorbed fluence of 2000 J/m^2 in vacuum and in the presence of a 1 atm Ar gas environment. The irradiation regime in these simulations corresponds to the phase explosion in the top part of the target. Only parts of the computational system are shown in the snapshots. The Al atoms are colored according to their potential energies.

The expansion of the fine "Swiss cheese"-like cellular structure generated in an ~100 nm wide surface region of the target during the first 50 ps after the laser pulse [38] leads to the coarsening of

the liquid regions and eventual disintegration of the evolving foamy structure into individual liquid droplets (see snapshots for 200, 400, and 600 ps in Fig. 12.4). We can conclude that, under conditions of stress confinement realized in fs laser ablation of metals, the clusters and droplets generated in the phase explosion of the top part of the target and the ones emerging from photomechanical cavitation and disintegration of the deeper melted material have different characteristics and contribute to different parts of the ablation plume. The results of the cluster analysis shown Fig. 12.5 indicate that the front part of the expanding plume consists of vapor-phase atoms and small droplets, the medium part of the plume consists of medium-size droplets, and the rear part of the plume consists of large liquid droplets. This cluster segregation effect can be related to the results of plume imaging experiments [7, 8, 39, 40, 111-115], where the plume splitting into a fast component with an optical emission characteristic for neutral atoms and a slow component with blackbody-like emission of hot clusters is observed.

The occurrence of both spallation and phase explosion processes within the same laser spot (Fig. 12.2) can be related to the results of pump-probe experiments [116–118], where the observation of optical interference patterns (Newton rings) can be explained by the spallation of a thin liquid layer from the irradiated target, and the disappearance of the interference fringes in the central part of the laser spot [116–118] can be attributed to the transition to the phase explosion regime. Moreover, the sharp increase in the fraction of the vapor-phase atoms in the ablation plume upon the transition from spallation to phase explosion [38, 55, 110] can be related to the results of plume imaging experiments [111], where the maximum ejection of nanoparticles in laser ablation of Ni targets is observed at low fluences, whereas the degree of plume atomization increases at higher fluences. Note that the ejection of liquid layers observed in the simulations performed in the spallation regime can be related to the experimental observation of micro- and nanoparticles since the thin liquid layers can be expected to become unstable and decompose into individual droplets, as discussed in Ref. [38] on the basis of thin-film instability theory [119].

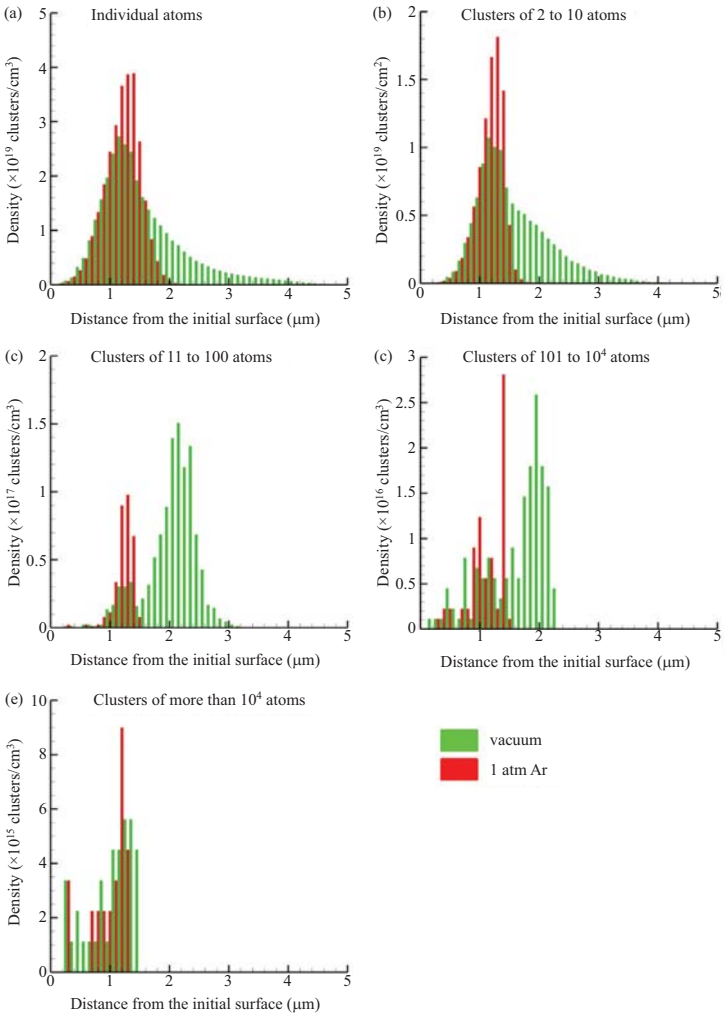

Figure 12.5 Number density of individual atoms (a) and clusters of different sizes (b–e) as a function of the distance from the initial surface in simulations of laser ablation of a bulk Al target irradiated by a 100 fs laser pulse at an absorbed fluence of 2000 J/m^2 with and without the presence of a 1 atm Ar background gas. The distributions are plotted for 600 ps after the laser pulse, which corresponds to the last pair of snapshots shown in Fig. 12.4. The analysis is performed for groups of clusters of similar sizes to obtain statistically adequate representations of the spatial distribution of clusters of different sizes in the ablation plume.

12.4 Ablation in a Background Gas

The presence of a background gas is recognized as a key factor enabling an effective control over nanoparticle structure and size distribution in short-pulse laser ablation, for example, Refs. [3, 4, 120–122]. Experimental probing of the ablation plume dynamics with various time- and spatially resolved optical and spectroscopic imaging techniques [3, 4, 8, 121–128] has provided a wealth of information on the evolution of different plume components and revealed a number of interesting phenomena, such as the plume splitting into fast and slow components, shock wave formation, onset of oscillatory behavior and turbulence, plume stagnation, and redeposition of ablated material.

A number of distinct regimes of ablation plume interaction with the background gas have been identified [122, 128, 129] and related to suitable theoretical models. At low pressure, up to about 1 Pa, the effect of scattering of the ablated species by the background gas is weak and the vacuum-like plume dynamics can be described as a self-similar adiabatic expansion [130]. The confining effect of the background gas becomes noticeable as the pressure approaches 10 Pa, when the plume shape starts to change [128], the angular distribution of the ablated species broadens [129], and the plume slows down. In this regime, the collective motion of the background gas due to the collisions with ablated species can still be neglected and the random scattering of the ablated species in the background gas can be simulated with the Monte Carlo computational technique [131, 132]. For intermediate pressure, between 10 and 100 Pa, a combination of scattering and collective motion leads to a complex interplay of compression and interpenetration of the plume and the background gas, thus presenting a challenge for a theoretical description. The empirical drag model [133], a model combining scattering and gas dynamic concepts [134], a mixed-propagation (diffusion and drag) model incorporating cluster growth kinetics [122, 135], and a combined Monte Carlo–hydrodynamic model [136] are among the approaches developed for the description of the ablation plume dynamic in this regime. Finally, for the background pressure of hundreds of pascals and higher, the shock wave formation and propagation dominate the plume dynamics and can be described by a “point explosion” analytical model [137–140]

or gas dynamics computational models that neglect the diffusional mixing [127, 141–143].

A complete picture of the ablation plume interaction with the background gas, including the formation of the plume–ambient gas mixing zone and the shock front characteristics, can be provided by MD simulations of the ablation process. While, in principle, MD simulations can be performed for any magnitude of the background pressure, the high computational cost of the simulations makes it practical to only consider the high pressures, when the active processes of the shock wave and mixing zone formation take place during the first nanoseconds after the laser pulse. Indeed, the first MD simulations of laser ablation in a background gas were performed for 0.03 to 8.6 atm [77–80] and provided important insights into the initial ablation plume dynamics, shock wave formation, and characteristics of the plume–ambient gas interaction zone.

An important advantage of the MD technique is the ability to account for the direct ejection of atomic clusters and liquid droplets from the targets irradiated by short laser pulses. It has been demonstrated in experiments [8, 14, 108, 144, 145] and predicted in MD simulations performed for metals and molecular systems [37, 38, 55, 59, 60, 76, 110] that the clusters/droplets are unavoidable products of the explosive material disintegration in short-pulse laser ablation and constitute a major fraction of the total mass of ejected material. Most of the theoretical and computational approaches developed for the description of laser ablation in a background gas and briefly discussed above, however, treat the initial state of the ejected material as a hot dense vapor and only consider the formation of clusters and nanoparticles through the collision-induced condensation in the dense regions of the ejected plume. A realistic representation of the material ejection in MD simulations, therefore, makes this technique uniquely suitable for the analysis of the implications of the multiphase composition of the ablation plume. The ability of MD simulations to reproduce the evolution of the cluster size distribution in the ablation plume interacting with a background gas is illustrated below by the results of a simulation of laser ablation of an Al target in a 1 atm Ar gas environment.

To facilitate a comparison with laser ablation in vacuum, the simulation of laser ablation in Ar gas is performed for the same absorbed fluence of 2000 J/m^2 and pulse duration of 100 fs as in one

of the simulations discussed above, in Section 12.3. The size of the Al sample is also the same, with a 4 μm thick Ar gas region added above the surface of the sample, as shown in Fig. 12.1. As can be seen from the snapshots shown in Fig. 12.4, the overall picture of the ablation process is similar in vacuum and in the 1 atm Ar gas. In both cases, the top surface regions of Al targets undergo explosive decomposition into mixtures of vapor and liquid droplets, while deeper regions undergo cavitation caused by the propagation of the tensile (unloading) components of the laser-induced pressure waves (see Section 12.3 for a discussion of the ablation mechanisms). However, one can still clearly observe the differences in the dynamics of the plume expansion. Even at the very early stage of the ablation process, at 200 ps after the laser pulse, there is a noticeable effect of the background gas on the expansion of the small liquid droplets, atomic clusters, and vapor-phase metal atoms generated in the phase explosion of the top surface layer of the target. The suppression of the expansion of the front part of the ablation plume becomes more pronounced with time and results in the formation of a well-defined layer of liquid droplets generated by the coalescence of small clusters and droplets decelerated by the interaction with the background gas. On the side of the background gas, the strong push from the ablation plume results in the shock wave formation in the Ar gas, with the temperature of the shocked Ar increasing up to more than 8000 K and the pressure behind the shock front reaching 80 atm.

The interaction of the plume with the compressed background gas has a dramatic effect on the cluster composition of the expanding plume as well as the spatial distribution of clusters in the plume, as can be seen from Fig. 12.5, where the distributions of vapor-phase atoms and clusters of different sizes are shown for a time of 600 ps after the laser pulse. The collisions of the metal atoms and small atomic clusters with the background gas atoms slow down the fastest plume species, reduce their total populations, and produce more narrow spatial distributions in Fig. 12.5a,b. The interaction of the ablation plume with the background gas results in the formation of a dense front layer of the plume, where collisions and coalescence of small droplets and clusters increase the population of intermediate and large droplets. The effect of the background gas is particularly strong on atomic clusters consisting of 11 to 100 atoms

(Fig. 12.5c) and small droplets consisting of up to 10,000 atoms (Fig. 12.5d), which are prominently present in the front part of the plume generated in the laser ablation in vacuum but almost completely eliminated by the plume interaction with the background gas. The larger droplets, with more than 10,000 atoms, are less affected by the background gas pressure, as most of them originate from the spallation process in the deeper part of the plume and do not directly interact with the Ar atoms during the time of the simulation.

While the strong effect of the background gas on the cluster composition of the ablation plume and the dynamics of different plume components is generally recognized and supported by experimental evidence [3, 4, 8, 120–122], the computational prediction of the short timescale of the drastic changes in the plume composition, occurring within the first nanosecond of the plume expansion, is rather startling and unexpected. Additional simulations performed at higher levels of background pressure (up to 10 atm, to be reported elsewhere) reveal the formation of an increasingly thick and continuous liquid layer at the interface with the shock-compressed background gas. The formation of the dense liquid layer at the front of the plume due to the spatial confinement of the plume by the background gas can be related to a similar phenomenon observed in simulations of laser ablation under much stronger confinement by a liquid environment, as discussed in the next section.

12.5 Ablation in Liquids

Pulse laser ablation in liquids (PLAL) has flourished since the early 2000s, when several groups successfully demonstrated the synthesis and size control of noble metal nanoparticles through PLAL [34, 36, 146, 147]. While the experimental setup in PLAL is simple, the liquid environment induces complicated plume–liquid interactions that not only define the nanoparticle size distribution but also facilitate the formation of metastable nanoparticles with unusual structures and composition [28–32, 148]. The size of the nanoparticles can be controlled by using different types of liquids [19–21], as well as by adding organic ligands [23–26] or inorganic salts [27] into the liquid. Moreover, a number of techniques based

on post-irradiation of colloidal solutions, such as laser melting in liquids and laser fragmentation in liquids, have been demonstrated to be effective in further modifying the size, shape, and composition of the nanoparticles [149–153]. The ability of PLAL to produce stable contamination-free colloidal solutions of nanoparticles makes this technique very attractive for various fields of application, including biomedicine [154] and chemical catalysis [155, 156]. While there are comprehensive reviews of the experimental progress in the development of PLAL [15–18, 157], the fundamental mechanisms of nanoparticle formation by laser ablation in liquids are still not fully understood.

The general picture of laser ablation in liquids is very different from the one in vacuum. The ablation plume does not expand freely but is confined by the liquid environment. The liquid in contact with the plume is quickly heated and vaporized to form a thin layer of vapor surrounding the plume. This thin vapor layer can be directly observed via shadowgraphy [158] or X-ray radiography [159] as a dark zone surrounding the plume. The supply of heat from the plume creates and maintains high-temperature and high-pressure conditions in the vapor layer and drives the expansion of the layer. The expansion of the vapor layer away from the target leads to the formation of a cavitation bubble, while the pressure it exerts in the opposite direction pushes against the ablation plume and suppresses its expansion. It is often observed that the cavitation bubble undergoes a series of expansion, contraction, and collapse cycles [159, 160]. The interpretation of experimental results on the evolution of the cavitation bubble is typically based on the Rayleigh-Plesset equation used in combination with the van der Waals equation of state [158–162]. The dynamics of the cavitation bubble expansion and collapse are expected to play a major role in the generation of nanoparticles in PLAL, although the exact mechanisms of nanoparticle formation have not been established yet.

Currently, an accepted view is that the ablated material is likely to be confined and trapped inside the cavitation bubble, where favorable pressure and temperature conditions for nanoparticle nucleation, growth, coalescence, and solidification are realized [163, 164]. This general scenario, however, cannot be directly verified and

detailed with conventional optical methods, since an optically dense interface between the liquid and the cavitation bubble blocks the view of the processes occurring inside the bubble. Recently, the novel use of small-angle X-ray scattering (SAXS) is demonstrated to be capable of relating the cavitation bubble dynamics to nanoparticle growth [159, 165]. In situ SAXS can be used to scan different positions in the bubble with different time delays, thus enabling mapping of the particle size distribution with respect to the time and position inside the bubble [159, 165, 166].

Signals yielded by SAXS have revealed two distinct nanoparticle size populations in the cavitation bubble: the "primary particles," with a size distribution centered around 8–10 nm, and the "secondary particles," with sizes around 50 nm. The primary particles are detected at the early stage of the first bubble expansion. A higher density of primary particles is detected near the bottom of the bubble, and their abundance decays toward the top of the bubble. The signal from the secondary particles is weak during the first cycle of the bubble expansion and collapse but becomes stronger after the rebound. The secondary particles are speculated to form due to the agglomeration of primary particles during the bubble collapse, when the primary particles are forced to collide with each other due to the sudden volume contraction. The sizes of the secondary particles are found to be highly variable, with rapid changes observed in the course of the bubble dynamics, suggesting that these "particles" may not be compact objects but some forms of loose networks of molten material or nanoparticle agglomerates. While the interpretation of SAXS data provides firsthand quantitative understanding of nanoparticle generation in PLAL, other approaches are needed to fully capture the nanoparticle generation mechanisms. In particular, atomic clusters and nanoparticles smaller than 5 nm cannot be detected with SAXS but may be responsible for the nanoparticle nucleation and growth in the ablation process, as well as the slower growth and coarsening of nanoparticles in the colloidal solutions generated by PLAL. Moreover, the primary particles detected at the early stage of the first bubble expansion are likely to be directly ejected from the irradiated target or formed during the first nanoseconds of the plume expansion, which is currently beyond the

temporal resolution of SAXS. One needs to push beyond the current SAXS limits on particle sizes and temporal/spatial resolution to observe the ablation phenomena in more detail. There is also a need to resolve the thermodynamic states of the plume confined in the cavitation bubble to enable a reliable theoretical description of PLAL.

Computational modeling can play an important role in the interpretation of experimental observations and exploration of mechanisms of the nanoparticle generation in PLAL. Only the first attempts to address the nanoparticle generation mechanisms in one-dimensional continuum-level hydrodynamic modeling, however, have been reported so far [44, 45]. The liquid in these simulations is assumed to be a transparent, thermally insulating, and nonmixable overlayer with mechanical properties described by a single-phase equation of state parametrized for water. The highly simplified representation of the water environment prevents the realistic description of some of the key processes, such as the formation of a layer of water vapor driving the expansion of the cavitation bubble, water–metal mixing, and rapid cooling of the metal species in the mixing region. Moreover, the one-dimensional nature of the model does not allow for the direct simulation of nanoparticle generation. Nevertheless, the results of the hydrodynamic simulations have provided important insights into the initial dynamics of laser ablation under conditions of spatial confinement by a liquid overlayer and demonstrated that the confinement alone can facilitate generation of nanoparticles with a bimodal size distribution. The predictions of these simulations are illustrated in Fig. 12.6, where the contour plots show the phase transformations in an Au target irradiated by a 200 fs laser pulse at two different laser fluences. In the low-fluence regime, the ejection of multiple liquid layers is observed (Fig. 12.6a) and attributed to the photomechanical spallation. The spalled layers merge into one thick layer due to the deceleration of the front layer, in contact with water. One can speculate that breakdown of this liquid layer in the course of the spallation process or due to the thin-film instability may produce nanoparticles comparable to the thickness of the spalled layers, of the order of tens of nanometers. At a higher laser fluence, the top layer of the irradiated target undergoes an explosive decomposition into a mixture of liquid droplets and vapor,

which pushes the water overlayer away from the target and creates a low-density region where small nanoparticles are expected to grow through condensation from the vapor phase.

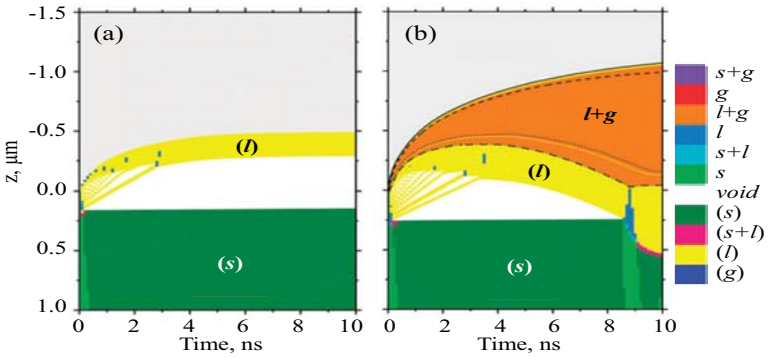

Figure 12.6 Time–space diagrams showing the phase composition of different regions of gold targets irradiated in a water environment by 200 fs laser pulses at absorbed fluences of 2600 J/m^2 (a) and 5500 J/m^2 (b), as predicted in continuum-level hydrodynamic simulations reported in Ref. [45].

As has been demonstrated above, in Sections 12.3 and 12.4, large-scale MD simulations are capable of not only predicting the thermodynamic conditions leading to the material ejection in laser ablation but also providing detailed atomic-level information on the mechanisms of nanoparticle formation. With the development of a computationally efficient coarse-grained representation of the liquid environment, discussed in Section 12.2.2, it is now possible to apply the MD technique to the simulation of PLAL, as has been demonstrated in recent MD simulations of thin Ag film ablation in water [106]. The extension of this work to a simulation of laser ablation of a bulk silver target in water is presented below and illustrated in Figs. 12.7–12.9. The schematic of the computational setup is provided in Fig. 12.1, with the depth of the atomistic TTM-MD part of the target, L_z, equal to 200 nm in the lower-fluence simulation (Fig. 12.7) and 400 nm at a higher fluence (Fig. 12.8); the size of the region where the coarse-grained representation of water overlayer is used, L_{env}, is 300 nm; the lateral dimensions of the computational cell are 100 nm × 100 nm; and the laser pulse duration is 100 fs.

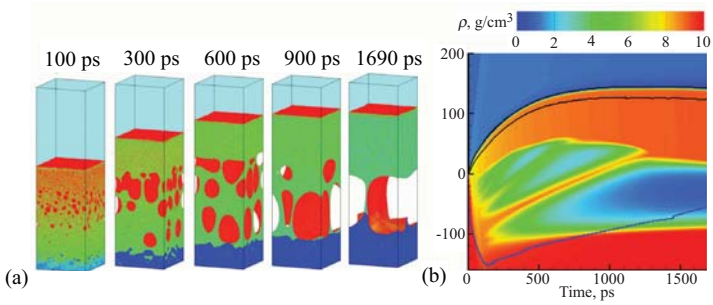

Figure 12.7 Snapshots of atomic configurations (a) and a density contour plot (b) predicted in the atomistic simulation of laser ablation of a bulk silver target irradiated in water by a 100 fs laser pulse at an absorbed fluence of 1500 J/m^2. Only parts of the computational system, from –160 to 200 nm with respect to the initial surface of the silver target, are shown in the snapshots. The atoms are colored according to their potential energies: from blue for the crystalline part of the target to green for liquid Ag and red for internal surfaces of the voids and the water–Ag interface. The molecules representing the water environment are blanked, and the presence of water is illustrated schematically as a bright-blue region above the Ag target. In the contour plot, the blue line shows the location of the melting and solidification fronts, while the two black lines outline the water–Ag mixing region, defined as a region where both water molecules and Ag atoms are present.

The absorbed fluence of 1500 J/m^2, used in the first simulation illustrated in Fig. 12.7, is about 50% above the spallation threshold for irradiation in vacuum [92], where the ejection of multiple liquid layers/droplets is observed (see Section 12.3 for the discussion of the spallation mechanism). The initial response of the Ag target to the laser excitation in the simulation of PLAL is similar to that in vacuum, with multiple voids nucleating, growing, and coalescing in the subsurface region of the target (Fig. 12.7a) in response to the generation of tensile stresses (Fig. 12.9a). The resistance of the water environment to the outward motion of the top layer, however, prevents the complete separation of the melted layer from the target, slows down the layer, and, at about 1.35 ns after the laser pulse, reverses the direction of its motion. The conductive cooling through the remaining liquid bridge connecting the top layer to the bulk of the target, combined with an additional cooling due to the interaction with water environment, brings the average temperature of the liquid layer down to the equilibrium melting temperature of the EAM Ag, T_m = 1139 K [52] by 740 ps after the laser pulse and

undercools the layer down to 0.85 T_m by the end of the simulation at 1690 ps. While the simulation was not continued beyond 1690 ps, it can be estimated from the rate of cooling and the velocity of the layer in the direction toward the surface that the connecting bridge and the entire layer will solidify well before the time that would be needed for redeposition of the liquid layer to the target. The solidification is expected to proceed by a combination of epitaxial regrowth of the single-crystal target through the bridge into the top layer (the front of the epitaxial regrowth is shown by the blue line in the contour plot in Fig. 12.7b) and a massive nucleation of new crystallites at ~4 ns, when the temperature of the layer T_m is projected to decrease to ~0.7 [56].

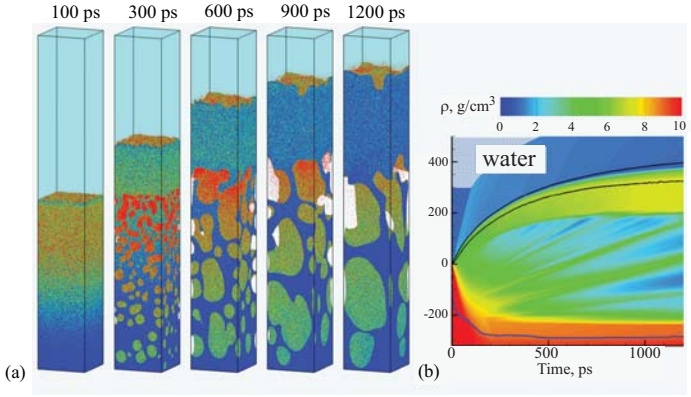

Figure 12.8 Snapshots of atomic configurations (a) and the density contour plot (b) predicted in atomistic simulation of laser ablation of a bulk silver target irradiated in water by a 100 fs laser pulse at an absorbed fluence of 4000 J/m^2. Only parts of the computational system, from –220 to 450 nm with respect to the initial surface of the silver target, are shown in the snapshots. The atoms are colored according to their potential energies, from blue for liquid Ag to red for the vapor-phase Ag atoms. The molecules representing the water environment are blanked, and the presence of water is illustrated schematically as a bright-blue region above the Ag target. In the contour plot, the blue line shows the location of the melting and solidification fronts, while the two black lines outline the water–Ag mixing region, defined as a region where both water molecules and Ag atoms are present.

The computational prediction of the formation of large subsurface voids, stabilized by the rapid cooling and solidification of the surface region, has important implications for both generation of nanoparticles in a multipulse irradiation regime and surface mod-

ification by laser processing in a liquid environment. The subsurface voids generated by laser spallation confined by water are many times larger than the ones observed close to the spallation threshold in vacuum [56]. The final structure expected to form after complete solidification in the simulation illustrated in Fig. 12.7a is essentially a thin metal layer loosely connected to the bulk of the target by thin walls and bridges. The irradiation of such a target by a subsequent laser pulse would result in the partial confinement of the deposited laser energy in the surface layer, leading to a substantial reduction of the threshold fluence for the onset of the phase explosion. Thus, while the generation of nanoparticles is not observed at this fluence upon the first pulse laser irradiation, the appearance of large subsurface voids can help to produce nanoparticles through the decomposition of the upper layer of the target upon irradiation by subsequent pulses, leading to the incubation effect for the nanoparticle generation demonstrated earlier in simulations performed in vacuum [56]. The incubation due to the presence of subsurface voids in pulsed laser ablation in liquids has also been observed in large-scale MD simulations and will be reported elsewhere.

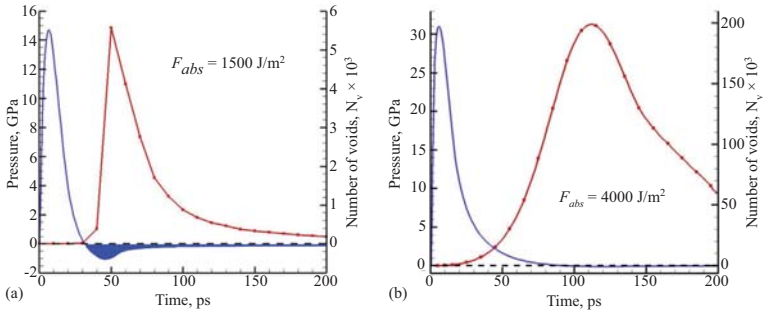

Figure 12.9 The evolution of pressure (blue curves) and the total number of voids (red curves) in atomistic simulations of 100 fs laser irradiation of Ag targets at absorbed fluences of 1500 J/m^2 (a) and 4000 J/m^2 (b). For both plots, the pressure is averaged over a region between 10 and 60 nm under the initial surface of the Ag target. The region of negative (tensile) pressure is colored blue in (a). The decrease in the number of voids is related to the void coalescence and coarsening, with the total volume of the voids rapidly increasing in both simulations during the time shown in the plots.

The stabilization of large subsurface voids and frozen surface structures by the interaction of the laser-generated transient melted structures with a liquid environment, predicted in the simulations,

is also consistent with experimental observations of distinct surface nanomorphologies generated in laser processing in liquids [121, 167–172]. Further improvement in the computational efficiency of the atomistic simulations and the development of new multiscale approaches are needed to enable an efficient computational exploration of surface nanostructuring in liquids at experimentally relevant length scales and timescales.

The second simulation, illustrated in Figs. 12.8 and 12.9b, is performed at a higher absorbed laser fluence of 4000 J/m^2, which is about two times the threshold fluence for the transition from spallation to phase explosion regimes of laser ablation in vacuum [92]. The superheated liquid that in vacuum undergoes an explosive decomposition into small liquid droplets and vapor is now confined by water and is collected into a dense hot layer that pushes the water away from the target. The layer grows as the porous subsurface region of the Ag target expands, and more melted and vapor-phase Ag join the layer. Note that despite the visual similarity of the subsurface void evolution in Figs. 12.7 and 12.8, the main driving forces behind the void generation in the two simulations are different, as can be clearly seen from Fig. 12.9. In the low-fluence regime, at the absorbed fluence of 1500 J/m^2, the sharp increase of the number of subsurface voids coincides with the time when tensile stresses, highlighted by blue color in Fig. 12.9a, are generated due to the relaxation of the initial compressive pressure. At the higher fluence of 4000 J/m^2, the superheated top layer confined by the water environment keeps the positive pressure on the underlying melted part of the target for a longer time (Fig. 12.9b). The generation of voids in this case is mainly driven by the release of vapor and can be described as homogeneous boiling.

At a later time, beyond the timescale of the simulation, the top Ag layer is expected to completely separate from the target and slowly cool down due to the interaction with water. The water–silver mixing region, outlined by two black lines in Fig. 12.8b, is expected to grow and evolve into a low-density vapor region expanding under the action of water vapor pressure. The condensation of Ag vapor in the mixing region is expected to result in the formation of small Ag clusters, as have been observed in simulations of thin-film ablation [106] as well as ablation of bulk targets that will be reported elsewhere. At the same time, the top liquid layer is likely to rupture

into larger liquid droplets due to the inherent instability of thin liquid films [38, 119] and the dynamic interaction of the liquid layer with the expanding and collapsing vapor bubble. The coexistence of the two distinct mechanisms of nanoparticle formation, the nucleation and growth in the mixing region and the decomposition of the thin liquid layer [106], may be related to the common observation of bimodal nanoparticle size distributions in PLAL [34, 36].

12.6 Concluding Remarks

The advancement of computational methods for the simulation of laser interactions with materials and the fast growth of available computing resources are expanding the range of research problems that can be addressed in large-scale MD simulations. Recent developments of computationally efficient approaches to the description of laser ablation in the presence of a background gas or liquid environment have enabled an exploration of the effect of various degrees of spatial confinement on the material response to short-pulse laser irradiation and generation of nanoparticles in laser ablation.

The comparison of the results of large-scale atomistic simulations of laser ablation of Al targets in vacuum and in a 1 atm Ar gas environment has revealed a surprisingly strong effect of the background gas on the initial plume expansion and evolution of the cluster size distribution. The formation of a strong shock wave in Ar, the rapid coalescence of smaller droplets and clusters in the dense front part of the ablation plume, and the suppression of the generation of small and medium-size Al clusters are among the effects predicted in the simulations.

The effect of a much stronger confinement of the ablation process by a liquid environment is explored in MD simulations of laser spallation and ablation of Ag targets in water. In the spallation regime, the confinement by a water environment is found to prevent the complete separation of the spalled layers from the target, leading to the stabilization of large subsurface voids frozen in a rapid solidification process and suggesting the incubation effect for the generation of nanoparticles. The computational prediction of the formation of a porous surface region with a complex morphology of frozen subsurface structures can also be related to experimental

observations of distinct surface nanomorphologies generated in laser processing in liquids. At a higher laser fluence, which results in the phase explosion in vacuum, the confinement by water suppresses the phase decomposition of the superheated top layer of the target and collects the ejected material into a dense hot layer that pushes the water away from the target.

While the simulations reported in this chapter demonstrate the ability of the MD simulations to provide important insights into the mechanisms of laser interactions with metals in different environments, further advancements in the computational efficiency of MD simulations and the development of new multiscale approaches are needed to enable effective computational exploration of the longer-term processes of mixing of the ablation plume with a liquid environment, cavitation bubble formation, and surface nanostructuring in liquids at experimentally relevant length- and timescales.

Acknowledgments

Financial support for this work was provided by the National Science Foundation (NSF) through Grants CMMI-1301298, CMMI-1436775, and DMR-1610936, as well as the Austrian Science Fund (FWF) through the Lise Meitner Programme (project M 1984). Computational support was provided by the Oak Ridge Leadership Computing Facility (INCITE project MAT130) and NSF through the Extreme Science and Engineering Discovery Environment (Project TG-DMR110090).

References

1. Barcikowski, S., Hahn, A., Kabashin, A. V., and Chickhov, B. N. (2007). Properties of nanoparticles generated during femtosecond laser machining in air and water, *Appl. Phys. A*, **87**, pp. 47–55.
2. Ruffino, F., Pugliara, A., Carria,E., Romano, L., Bongiorno, C., Spinella, C., and Grimaldi, M. G. (2012). Novel approach to the fabrication of Au/silica core–shell nanostructures based on nanosecond laser irradiation of thin Au films on Si, *Nanotechnology*, **23**, p. 045601.
3. Geohegan, D. B., Puretzky, A. A., Duscher, G., and Pennycook, S. J. (1998). Time-resolved imaging of gas phase nanoparticle synthesis by laser ablation, *Appl. Phys. Lett.*, **72**, pp. 2987–2989.

4. Umezu, I., Sugimura, A., Inada, M., Makino, T., Matsumoto, K., and Takata, M. (2007). Formation of nanoscale fine-structured silicon by pulsed laser ablation in hydrogen background gas, *Phys. Rev. B*, **76**, p. 045328.
5. Jo, Y. K., and Wen, S. B. (2011). Direct generation of core/shell nanoparticles from double-pulse laser ablation in a background gas, *J. Phys. D: Appl. Phys.*, **44**, p. 305301.
6. Umezu, I., Sakamoto, N., Fukuoka, H., Yokoyama, Y., Nobuzawa, K., and Sugimura, A. (2013). Effects of collision between two plumes on plume expansion dynamics during pulsed laser ablation in background gas, *Appl. Phys. A*, **110**, pp. 629–632.
7. Amoruso, S., Bruzzese, R., Wang, X., Nedialkov, N. N., and Atanasov, P. A. (2007). Femtosecond laser ablation of nickel in vacuum, *J. Phys. D: Appl. Phys.*, **40**, pp. 331–340.
8. Amoruso, S., Bruzzese, R., Wang, X., and Xia, J. (2008). Propagation of a femtosecond pulsed laser ablation plume into a background atmosphere, *Appl. Phys. Lett.*, **92**, p. 041503.
9. Chichkov, B. N., Momma, C., Nolte, S., Alvensleben, F. V., and Tunnermann, A. (1996). Femtosecond, picosecond and nanosecond laser ablation of solids, *Appl. Phys. A*, **63**, pp. 109–115.
10. Rethfeld, B., Sokolowski-Tinten, K., Von Der Linde, D., and Anisimov, S. I. (2004). Timescale in the response of materials to femtosecond laser excitation, *Appl. Phys. A*, **79**, pp. 767–769.
11. Amoruso, S., Nedyalkov, N. N., Wang, X., Ausanio, G., Bruzzese, R., and Atanasov, P. A. (2011). Ultrafast laser ablation of gold thin film targets, *J. Appl. Phys.*, **110**, p. 124303.
12. Oguri, K., Okano, Y., Nishikawa, T., and Nakano, H. (2009). Dynamics of femtosecond laser ablation studied with time-resolved x-ray absorption fine structure imaging, *Phys. Rev. B*, **79**, p. 144106.
13. Haustrup, N., and O'Connor, G. M. (2012). Impact of wavelength dependent thermo-elastic laser ablation mechanism on the generation of nanoparticles from thin gold films, *Appl. Phys. Lett.*, **101**, p. 263107.
14. Donnelly, T., Lunney, J. G., Amoruso, S., Bruzzese, R., Wang, X., and Ni, X. (2010). Dynamics of the plumes produced by ultrafast laser ablation of metals, *J. Appl. Phys.*, **108**, p. 043309.
15. Asahi, T., Mafune, F., Rehbock, C., and Barcikowski, S. (2015). Strategies to harvest the unique properties of laser-generated nanomaterials in biomedical and energy applications, *Appl. Surf. Sci.*, **348**, pp. 1–3.

16. Rehbock, C., Jakobi, J., Gamrad, L., van der Meer, S., Tiedemann, D., Taylor, U., Kues, W., Rath, D., and Barcikowski, S. (2014). Current state of laser synthesis of metal and alloy nanoparticles as ligand-free reference materials for nano-toxicological assays, *Beilstein J. Nanotechnol.*, **5**, pp. 1523–1541.
17. Yang, G. W. (2007). Laser ablation in liquids: application in the synthesis of nanocrystals, *Prog. Mater. Sci.*, **52**, pp. 648–698.
18. Tarasenko, N. V., and Butsen, A. V. (2010). Laser synthesis and modification of composite nanoparticles in liquids, *Quantum Electron.*, **40**, pp. 986–1003.
19. Tilaki, R. M., Iraji Zad, A., and Mahdavi, S. M. (2006). Stability, size and optical properties of silver nanoparticles prepared by laser ablation in different carrier media, *App. Phys. A*, **84**, pp. 215–219.
20. Bärsch, N., Jakobi, J., Weiler, S., and Barcikowski, S. (2009). Pure colloidal metal and ceramic nanoparticles from high-power picosecond laser ablation in water and acetone, *Nanotechnology*, **20**, p. 445603.
21. Gökce, B., VantZand, D. D., Menendez-Manjon, A., and Barcikowski, S. (2015). Ripening kinetic of laser-generated plasmonic nanoparticle in different solvents, *Chem. Phys. Lett.*, **626**, pp. 96–101.
22. Menendez-Manjon, A., Chichkov, B., and Barcikowski, S. (2010). Influence of water temperature on the hydrodynamic diameter of gold nanoparticles from laser ablation, *J. Phys. Chem. C*, **114**, pp. 2499–2504.
23. Mafuné, F., Kohno, J.-Y., Takeda, Y., Kondow, T., and Sawabe, H. (2001). Formation of gold nanoparticles by laser ablation in aqueous solution of surfactant, *J. Phys. Chem. B*, **105**, pp. 5114–5120.
24. Compagnini, G., Scalisi, A. A., Puglisi, O., and Spinella, C. (2004). Synthesis of gold colloids by laser ablation in thiol-alkane solutions, *J. Mater. Res.*, **19**, pp. 2795–2798.
25. Sylvestre, J. P., Kabashin, A. V., Sacher, E., Meunier, M., and Luong, J. H. T. (2004). Stabilization and size control of gold nanoparticles during laser ablation in aqueouscyclodextrins, *J. Am. Chem. Soc.*, **126**, pp. 7176–7177.
26. Tsuji, T., Thang, D.-H., Okazaki, Y., Nakanishi, M., Tsuboi, Y., and Tsuji, M. (2008). Preparation of silver nanoparticle by laser ablation in polyvinylpyrrolidone solutions, *Appl. Surf. Sci.*, **254**, pp. 5224–5230.
27. Rehbock, C., Merk, V., Gamrad, L., Streubel, R., and Barcikowski, S. (2013). Size control oflaser-fabricated surfactant-free gold nanoparticles with highly diluted electrolytes and their subsequent bioconjugation, *Phys. Chem. Chem. Phys.*, **15**, pp. 3057–3067.

28. Yan, Z., Compagnini, G., and Chrisey, D. B. (2011). Generation of AgCl cubes by excimer ablation of bulk Ag in aqueous NaCl solutions, *J. Phys. Chem. C*, **115**, pp. 5058–5062.

29. Yan, Z., Bao, R., Huang, Y., and Chrisey, D. B. (2010). Hollow particles formed on laser-induced bubbles by excimer laser ablation in liquid, *J. Phys. Chem. C*, **114**, pp. 11370–11374.

30. Yan, Z., Bao, R., and Chrisey, D. B. (2011). Hollow nanoparticle generation on laser-induced cavitation bubbles via bubble interface pinning, *Appl. Phys. Lett.*, **97**, p. 124106.

31. Zhang, D., Gökce, B., Notthoff, C., and Barcikowski, S. (2015). Layered seed-growth of AgGe football-like mircospheres via precursor-free picosecond laser synthesis in water, *Sci. Rep.*, **5**, p. 13661.

32. Pearce, S. R. J., Henley, S. J., Claeyssens, F., May, P. W., Hallam, K. R., Smith, J. A., and Rosser, K. N. (2004). Production of nanocrystalline diamond by laser ablation at the solid/liquid interface, *Diamond Relat. Mater.*, **13**, pp. 661–665.

33. Streubel, R., Barcikowski, S., and Gökce, B. (2016). Continuous multigram nanoparticle synthesis by high-power, high-repetition-rate ultrafast laser ablation in liquids, *Opt. Lett.*, **41**, pp. 1486–1489.

34. Kabashin, A. V., and Meunier, M. (2003). Synthesis of colloidal nanoparticle during femtosecond laser ablation of gold in water, *J. Appl. Phys.*, **94**, pp. 7941–7943.

35. Rouleau, C. M., Shih, C.-Y., Wu, C., Zhigilei, L. V., Puretzky, A. A., and Geohegan, D. B. (2014). Nanoparticle generation and transport resulting from femtosecond laser ablation of ultrathin metal films: time-resolved measurements and molecular dynamics simulations, *Appl. Phys. Lett.*, **104**, p. 193106.

36. Sylvestre, J.-P., Kabashin, A. V., Sacher, E., and Meunier, M. (2005). Femtosecond laser ablation of gold in water: influence of the laser-produced plasma on the nanoparticle size distribution, *Appl. Phys. A*, **80**, pp. 753–758.

37. Zhigilei, L. V. (2003). Dynamics of the plume formation and parameters of the ejected clusters in short-pulse laser ablation, *Appl. Phys. A*, **76**, pp. 339–350.

38. Wu, C., and Zhigilei, L. V. (2014). Microscopic mechanisms of laser spallation and ablation of metal targets from large-scale molecular dynamics simulations, *Appl. Phys. A*, **114**, pp. 11–32.

39. Noel, S., Hermann, J., and Itina, T. (2007). Investigation of nanoparticle generation during femtosecond laser ablation of metals, *Appl. Surf. Sci.*, **253**, pp. 6310–6315.

40. Itina, T. E., Gouriet, K., Zhigilei, L. V., Noël, S., Hermann, J., and Sentis, M. (2007). Mechanisms of small clusters production by short and ultra-short pulse laser ablation, *Appl. Surf. Sci.*, **253**, pp. 7656–7661.

41. Paltauf, G., and Dyer, P. E. (2003). Photomechanical processes and effects in ablation, *Chem. Rev.*, **103**, pp. 487–518.

42. Leveugle, E., Ivanov, D. S., and Zhigilei, L. V. (2004). Photomechanical spallation of molecular and metal targets: molecular dynamics study, *Appl. Phys. A*, **79**, pp. 1643–1655.

43. Itina, T. E. (2011). On nanoparticle formation by laser ablation in liquids, *J. Phys. Chem. C*, **115**, pp. 5044–5048.

44. Povarnitsyn, M. E., and Itina, T. E. (2014). Hydrodynamic modeling of femtosecond laser ablation of metals in vacuum and in liquid, *Appl. Phys. A*, **117**, pp. 175–178.

45. Povarnitsyn, M. E., Itina, T. E., Levashov, P. R., and Khishchenko, K. V. (2013). Mechanisms of nanoparticle formation by ultra-short laser ablation of metals in liquid environment, *Phys. Chem. Chem. Phys.*, **15**, pp. 3108–3114.

46. Richardson, C. F., and Clancy, P. (1991). Picosecond laser processing of copper and gold: a computer simulation study, *Mol. Sim.*, **7**, pp. 335–355.

47. Hakkinen, H., and Landman, U. (1993). Superheating, melting, and annealing of copper surfaces, *Phys. Rev. Lett.*, **71**, pp. 1023–1026.

48. Ivanov, D. S., and Zhigilei, L. V. (2003). Combined atomistic-continuum modeling of short pulse laser melting and disintegration of metal films, *Phys. Rev. B*, **68**, p. 064114.

49. Ivanov, D. S., and Zhigilei, L. V. (2003). The effect of pressure relaxation on the mechanisms of short pulse laser melting, *Phys. Rev. Lett.*, **91**, p. 105701.

50. Lin, Z., and Zhigilei, L. V. (2006). Time-resolved diffraction profiles and atomic dynamics in short pulse laser induced structural transformations: molecular dynamics study, *Phys. Rev. B*, **73**, p. 184113.

51. Lin, Z., Johnson, R. A., and Zhigilei, L. V. (2008). Computational study of the generation of crystal defects in a bcc metal target irradiated by short laser pulses, *Phys. Rev. B*, **77**, p. 214108.

52. Wu, C., Thomas, D. A., Lin, Z., and Zhigilei, L. V. (2011). Runaway lattice-mismatched interface in an atomistic simulation of femtosecond laser irradiation of Ag film - Cu substrate system, *Appl. Phys. A*, **104**, pp. 781–792.

53. Thomas, D. A., Lin, Z., Zhigilei, L. V., Gurevich, E. L., Kittel, S., and Hergenröder, R. (2009). Atomistic modeling of femtosecond laser-induced melting and atomic mixing in Au film - Cu substrate system, *Appl. Surf. Sci.*, **255**, pp. 9605–9612.

54. Lin, Z., Bringa, E. M., Leveugle, E., and Zhigilei, L. V. (2010). Molecular dynamics simulation of laser melting of nanocrystalline Au, *J. Phys. Chem. C*, **114**, pp. 5686–5699.

55. Zhigilei, L. V., Lin, Z., and Ivanov, D. S. (2009). Atomistic modeling of short pulse laser ablation of metals: connections between melting, spallation, and phase explosion, *J. Phys. Chem. C*, **113**, pp. 11892–11906.

56. Wu, C., Christensen, M. S., Savolainen, J.-M., Balling, P., and Zhigilei, L. V. (2015). Generation of sub-surface voids and a nanocrystalline surface layer in femtosecond laser irradiation of a single crystal Ag target, *Phys. Rev. B*, **91**, p. 035413.

57. Sedao, X., Shugaev, M. V., Wu, C., Douillard, T., Esnouf, C., Maurice, C., Reynaud, S., Pigeon, F., Garrelie, F., Zhigilei, L. V., and Colombier, J.-P. (2016). Growth twinning and generation of high-frequency surface nanostructures in ultrafast laser-induced transient melting and resolidification, *ACS Nano*, **10**, pp. 6995–7007.

58. Anisimov, S. I., Zhakhovskii, V. V., Inogamov, N. A., Nishihara, K., Oparin, A. M., and Petrov, Yu. V. (2003). Destruction of a solid film under the action of ultrashort laser pulse, *Pis'ma Zh. Eksp. Teor. Fiz.*, **77**, pp. 731. [*JETP Lett.*, **77**, pp. 606–610 (2003)].

59. Zhigilei, L. V., Leveugle, E., Garrison, B. J., Yingling, Y. G., and Zeifman, M. I. (2003). Computer simulations of laser ablation of molecular substrates, *Chem. Rev.*, **103**, pp. 321–348.

60. Zhigilei, L. V., and Garrison, B. J. (2000). Microscopic mechanisms of laser ablation of organic solids in the thermal and stress confinement irradiation regimes, *J. Appl. Phys.*, **88**, pp. 1281–1298.

61. Wu, C., and Zhigilei, L. V. (2016). Nanocrystalline and polyicosahedral structure of a nanospike generated on metal surface irradiated by a single femtosecond laser pulse, *J. Phys. Chem. C*, **120**, pp. 4438–4447.

62. Ohmura, E., Fukumoto, I., and Miyamoto, I. (1998). Molecular dynamics simulation of laser ablation of metal and silicon, *Int. J. Jpn Soc. Precis. Eng.*, **32**, pp. 248–253.

63. Herrmann, R. F. W., Gerlach, J., and Campbell, E. E. B. (1998). Ultrashort pulse laser ablation of silicon: an MD simulation study, *Appl. Phys. A*, **66**, pp. 35–42.

64. Wu, X., Sadeghi, M., and Vertes, A. (1998). Molecular dynamics of matrix assisted laser desorption of leucine enkephalin guest molecules from nicotinic acid host crystal, *J. Phys. Chem. B*, **102**, pp. 4770–4778.

65. Cheng, C., and Xu, X. (2005). Mechanisms of decomposition of metal during femtosecond laser ablation, *Phys. Rev. B*, **72**, p. 165415.

66. Wang, X. W., and Xu, X. F. (2002). Molecular dynamics simulation of heat transfer and phase change during laser material interaction, *J. Heat Transfer*, **124**, pp. 265–274.

67. Lorazo, P., Lewis, L. J., and Meunier, M. (2006). Thermodynamic pathways to melting, ablation, and solidification in absorbing solids under pulsed laser irradiation, *Phys. Rev. B*, **73**, p. 134108.

68. Nedialkov, N. N., Atanasov, P. A., Imamova, S. E., Ruf, A., Berger, P., and Dausinger, F. (2004). Dynamics of the ejected material in ultra-short laser ablation of metals, *Appl. Phys. A*, **79**, pp. 1121–1125.

69. Anisimov, S. I., Zhakhovskii, V. V., Inogamov, N. A., Nishihara, K., Petrov, Y. V., Khokhlov, V. A. (2006). Ablated matter expansion and crater formation under the action of ultrashort laser pulse, *J. Exp. Theor. Phys.*, **103**, pp. 183–197.

70. Zhigilei, L. V., Kodali, P. B. S., and Garrison, B. J. (1997). Molecular dynamics model for laser ablation of organic solids, *J. Phys. Chem. B*, **101**, pp. 2028–2037.

71. Zhigilei, L. V., Kodali, P. B. S., and Garrison, B. J. (1997). On the threshold behavior in the laser ablation of organic solids, *Chem. Phys. Lett.*, **276**, pp. 269–273.

72. Zhigilei, L. V., and Garrison, B. J. (1999). Mechanisms of laser ablation from molecular dynamics simulations: dependence on the initial temperature and pulse duration, *Appl. Phys. A*, **69**, pp. S75–S80.

73. Yingling, Y. G., Zhigilei, L. V., and Garrison, B. J. (2001). The role of photochemical fragmentation in laser ablation: a molecular dynamics study, *J. Photochem. Photobiol. A*, **145**, pp. 173–181.

74. Schäfer, C., Urbassek, H. M., and Zhigilei, L. V. (2002). Metal ablation by picosecond laser pulses: a hybrid simulation, *Phys. Rev. B*, **66**, p. 115404.

75. Zhigilei, L. V., Yingling, Y. G., Itina, T. E., Schoolcraft, T. A., and Garrison, B. J. (2003). Molecular dynamics simulations of matrix assisted laser desorption - connections to experiment, *Int. J. Mass Spectrom.*, **226**, pp. 85–106.

76. Leveugle, E., and Zhigilei, L. V. (2007). Molecular dynamics simulation study of the ejection and transport of polymer molecules in matrix-assisted pulsed laser evaporation, *J. Appl. Phys.*, **102**, p. 074914.

77. Gacek, S., and Wang, X. (2008). Secondary shock wave in laser-material interaction, *J. Appl. Phys.*, **104**, p. 126101.

78. Gacek, S., and Wang, X. (2009). Dynamics evolution of shock waves in laser–material interaction, *Appl. Phys. A*, **94**, pp. 675–690.

79. Guo, L. Y., and Wang, X. W. (2009). Effect of molecular weight and density of ambient gas on shock wave in laser-induced surface nanostructuring, *J. Phys. D: Appl. Phys.*, **42**, p. 015307.

80. Li, C., Zhang, J. C., and Wang, X. W. (2013). Phase change and stress wave in picosecond laser-material interaction with shock wave formation, *Appl. Phys. A*, **112**, pp. 677–687.

81. Demaske, B. J., Zhakhovsky, V. V., Inogamov, N. A., and Oleynik, I. I. (2010). Ablation and spallation of gold films irradiated by ultrashort laser pulses, *Phys. Rev. B*, **82**, p. 064113.

82. Gill-Comeau, M., and Lewis, L. J. (2011). Ultrashort-pulse laser ablation of nanocrystalline aluminum, *Phys. Rev. B*, **84**, p. 224110.

83. Zhigilei, L. V., Lin, Z., Ivanov, D. S., Leveugle, E., Duff, W. H., Thomas, D., Sevilla, C., and Guy, S. J. (2010). Atomic/molecular-level simulations of laser-materials interactions, in *Laser-Surface Interactions for New Materials Production: Tailoring Structure and Properties*, eds. Miotello, A., and Ossi, P. M., Springer Series in Materials Science (Springer-Verlag, New York), Vol. 130, pp. 43–79.

84. Wu, C., Karim, E. T., Volkov, A. N., and Zhigilei, L. V. (2014). Atomic movies of laser-induced structural and phase transformations from molecular dynamics simulations, in *Lasers in Materials Science*, eds. Castillejo, M., Ossi, P. M., and Zhigilei, L. V., Springer Series in Materials Science (Springer International, Switzerland), Vol. 191, pp. 67–100.

85. Karim, E. T., Wu, C., and Zhigilei, L. V. (2014). Molecular dynamics simulations of laser-materials interactions: general and material-specific mechanisms of material removal and generation of crystal defects, in *Fundamentals of Laser-Assisted Micro- and Nanotechnologies*, eds. Veiko, V. P., and Konov, V. I., Springer Series in Materials Science (Springer International, Switzerland), Vol. 195, pp. 27–49.

86. Perez, D., Béland, L. K., Deryng, D., Lewis, L. J., and Meunier, M. (2008). Numerical study of the thermal ablation of wet solids by ultrashort laser pulses, *Phys. Rev. B*, **77**, p. 014108.

87. Kaganov, M. I., Lifshitz, I. M., and Tanatarov, L. V. (1957). Relaxation between electrons and crystalline lattices, *Sov. Phys. JETP*, **4**, pp. 173–178.

88. Anisimov, S. I., Kapeliovich, B. L., and Perel'man, T. L. (1974). Electron emission from metal surfaces exposed to ultrashort laser pulses, *Sov. Phys. JETP*, **39**, pp. 375–377.

89. Zhigilei, L. V., and Garrison, B. J. (1999). Pressure waves in microscopic simulations of laser ablation, *Mat. Res. Soc. Symp. Proc.*, **538**, pp. 491–496.

90. Schäfer, C., Urbassek, H. M., Zhigilei, L. V., and Garrison, B. J. (2002). Pressure-transmitting boundary conditions for molecular dynamics simulations, *Comp. Mater. Sci.*, **24**, pp. 421–429.

91. Zhigilei, L. V., and Ivanov, D. S. (2005). Channels of energy redistribution in short-pulse laser interactions with metal targets, *Appl. Surf. Sci.*, **248**, pp. 433–439.

92. Karim, E. T., Shugaev, M., Wu, C., Lin, Z., Hainsey, R. F., and Zhigilei, L. V. (2014). Atomistic simulation study of short pulse laser interactions with a metal target under conditions of spatial confinement by a transparent overlayer, *J. Appl. Phys.*, **115**, p. 183501.

93. Foiles, S. M. (1996). Embedded-atom and related methods for modeling metallic systems, *MRS Bull.*, **21**, pp. 24–28.

94. Mishin, Y., Farkas, D., Mehl, M. J., and Papaconstantopoulos, D. A. (1999). Interatomic potentials for monoatomic metals from experimental data and ab initio calculations, *Phys. Rev. B*, **59**, pp. 3393–3407.

95. Purja Pun, G. P., and Mishin, Y. (2009). Development of an interatomic potential for the Ni-Al system, *Phil. Mag.*, **89**, pp. 3245–3267.

96. Foiles, S. M., Baskes, M. I., and Daw, M. S. (1986). Embedded-atom-method functions for the fcc metals Cu, Ag, Au, Ni, Pd, Pt, and their alloys, *Phys. Rev. B*, **33**, pp. 7983–7991.

97. Lin, Z., and Zhigilei, L. V. (2006). Thermal excitation of d band electrons in Au: implications for laser-induced phase transformations, *Proc. SPIE*, **6261**, p. 62610U.

98. Lin, Z., and Zhigilei, L. V. (2007). Temperature dependences of the electron-phonon coupling, electron heat capacity and thermal conductivity in Ni under femtosecond laser irradiation, *Appl. Surf. Sci.*, **253**, pp. 6295–6300.

99. Lin, Z., Zhigilei, L. V., and Celli, V. (2008). Electron-phonon coupling and electron heat capacity of metals under conditions of strong electron-phonon nonequilibrium, *Phys. Rev. B*, **77**, p. 075133.

100. Matyushov, D. V., and Schmid, R. (1996). Calculation of Lennard-Jones energies of molecular fluids, *J. Chem. Phys.*, **104**, pp. 8627–8638.

101. Niu, W. X., and Zhang, H. (2012). Ar adsorptions on Al (111) and Ir (111) surfaces: a first-principles study, *Chin. Phys. B*, **21**, p. 026802.

102. Ziegler, J. F., Biersack, J. P., and Littmark, U. (1985). *The Stopping and Range of Ions in Solids* (Pergamon Press, New York).

103. Phares, D. J., and Srinivasa, A. R. (2004). Molecular dynamics with molecular temperature, *J. Phys. Chem. A*, **108**, pp. 6100–6108.

104. Jacobs, W. M., Nicholson, D. A., Zemer, H., Volkov, A. N., and Zhigilei, L. V. (2012). Acoustic energy dissipation and thermalization in carbon nanotubes: atomistic modeling and mesoscopic description, *Phys. Rev. B*, **86**, p. 165414.

105. Tabetah, M., Matei, A., Constantinescu, C., Mortensen, N. P., Dinescu, M., Schou, J., and Zhigilei, L. V. (2014). The minimum amount of "matrix" needed for matrix-assisted pulsed laser deposition of biomolecules, *J. Phys. Chem. B*, **118**, pp. 13290–13299.

106. Shih, C.-Y., Wu, C., Shugaev, M. V., and Zhigilei, L. V. (2016). Atomistic modeling of nanoparticle generation in short pulse laser ablation of thin metal films in water, *J. Colloid Interface Sci.*, **489**, pp. 3–17.

107. Miotello, A., and Kelly, R. (1999). Laser-induced phase explosion: new physical problems when a condensed phase approaches the thermodynamic critical temperature, *Appl. Phys. A*, **69**, pp. S67–S73.

108. Bulgakova, N. M., and Bulgakov, A. V. (2001). Pulsed laser ablation of solids: transition from normal vaporization to phase explosion, *Appl. Phys. A*, **73**, pp. 199–208.

109. Garrison, B. J., Itina, T. E., and Zhigilei, L. V. (2003). The limit of overheating and the threshold behavior in laser ablation, *Phys. Rev. E*, **68**, p. 041501.

110. Karim, E. T., Lin, Z., and Zhigilei, L. V. (2012). Molecular dynamics study of femtosecond laser interactions with Cr targets, *AIP Conf. Proc.*, **1464**, pp. 280–293.

111. Amoruso, S., Bruzzese, R., Pagano, C., and Wang, X. (2007). Features of plasma plume evolution and material removal efficiency during femtosecond laser ablation of nickel in high vacuum, *Appl. Phys. A*, **89**, pp. 1017–1024.

112. Albert, O., Roger, S., Glinec, Y., Loulergue, J. C., Etchepare, J., Boulmer-Leborgne, C., Perriere, J., and Millon, E. (2003). Time-resolved spectroscopy measurements of a titanium plasma induced by nanosecond and femtosecond lasers, *Appl. Phys. A*, **76**, pp. 319–323.

113. Jegenyes, N., Etchepare, J., Reynier, B., Scuderi, D., Dos-Santos, A., and Tóth, Z. (2008). Time-resolved dynamics analysis of nanoparticles applying dual femtosecond laser pulses, *Appl. Phys. A*, **91**, pp. 385–392.

114. Okano, Y., Oguri, K., Nishikawa, T., and Nakano, H. (2006). Observation of femtosecond-laser-induced ablation plumes of aluminum using space- and time-resolved soft X-ray absorption spectroscopy, *Appl. Phys. Lett.*, **89**, p. 221502.

115. Nakano, H., Oguri, K., Okano, Y., and Nishikawa, T. (2010). Dynamics of femtosecond-laser-ablated liquid-aluminum nanoparticles probed by means of spatiotemporally resolved X-ray absorption spectroscopy, *Appl. Phys. A*, **101**, pp. 523–531.

116. Agranat, M. B., Anisimov, S. I., Ashitkov, S. I., Zhakhovskii, V. V., Inogamov, N. A., Nishihara, K., Petrov, Yu. V., Fortov, V. E., and Khokhlov, V. A. (2007). Dynamics of plume and crater formation after action of femtosecond laser pulse, *Appl. Surf. Sci.*, **253**, pp. 6276–6282.

117. Sokolowski-Tinten, K., Bialkowski, J., Cavalleri, A., von der Linde, D., Oparin, A., Meyer-ter-Vehn, J., and Anisimov, S. I. (1998). Transient states of matter during short pulse laser ablation, *Phys. Rev. Lett.*, **81**, pp. 224–227.

118. Ionin, A. A., Kudryashov, S. I., Seleznev, L. V., and Sinitsyn, D. V. (2011). Dynamics of the spallative ablation of a GaAs surface irradiated by femtosecond laser pulses, *JETP Lett.*, **94**, pp. 753–758.

119. Vrij, A. (1966). Possible mechanism for the spontaneous rupture of thin, free liquid films, *Discuss. Faraday Soc.*, **42**, pp. 23–33.

120. Amoruso, S., Tuzi, S., Pallotti, D. K., Aruta, C., Bruzzese, R., Chiarella, F., Fittipaldi, R., Lettieri, S., Maddalena, P., Sambri, A., Vecchione, A., and Wang, X. (2013). Structural characterization of nanoparticles-assembled titanium dioxide films produced by ultrafast laser ablation and deposition in background oxygen, *Appl. Surf. Sci.*, **270**, pp. 307–311.

121. De Giacomo, A., Dell'Aglio, M., Gaudiuso, R., Amoruso, S., and De Pascale, O. (2012). Effects of the background environment on formation, evolution and emission spectra of laser-induced plasmas, *Spectrochim. Acta B*, **78**, pp. 1–19.

122. Ossi, P. M., Agarwal, N. R., Fazio, E., Neri, F., and Trusso, S. (2014). Laser-mediated nanoparticle synthesis and self-assembling, in *Lasers in Materials Science*, eds. Castillejo, M., Ossi, P. M., and Zhigilei, L. V., Springer Series in Materials Science (Springer International, Switzerland), Vol. 191, pp. 175–212.

123. Geohegan, D. B., and Puretzky, A. A. (1995). Dynamics of laser ablation plume penetration through low pressure background gases, *Appl. Phys. Lett.*, **67**, pp. 197–199.

124. Harilal, S. S., Bindhu, C. V., Tillack, M. S., Najmabadi, F., and Gaeris, A. C. (2003). Internal structure and expansion dynamics of laser ablation plumes into ambient gases, *J. Appl. Phys.*, **93**, pp. 2380–2388.

125. Freeman, J. R., Harilal, S. S., Diwakar, P. K., Verhoff, B., and Hassanein, A. (2013). Comparison of optical emission from nanosecond and femtosecond laser produced plasma in atmosphere and vacuum conditions, *Spectrochim. Acta B*, **87**, pp. 43–50.

126. Porneala, C., and Willis, D. A. (2006). Observation of nanosecond laser-induced phase explosion in aluminum, *Appl. Phys. Lett.*, **89**, p. 211121.

127. Miloshevsky, A., Harilal, S. S., Miloshevsky, G., and Hassanein, A. (2014). Dynamics of plasma expansion and shockwave formation in femtosecond laser-ablated aluminum plumes in argon gas at atmospheric pressures, *Phys. Plasmas*, **21**, p. 043111.

128. Diwakar, P. K., Harilal, S. S., Phillips, M. C., and Hassanein, A. (2015). Characterization of ultrafast laser-ablation plasma plumes at various Ar ambient pressures, *J. Appl. Phys.*, **118**, p. 043305.

129. Amoruso, S., Toftmann, B., and Schou, J. (2004). Thermalization of a UV laser ablation plume in a background gas: from a directed to a diffusionlike flow, *Phys. Rev. E*, **69**, p. 056403.

130. Anisimov, S. I., Bäuerle, D., and Luk'yanchuk, B. S. (1993). Gas dynamics and film profiles in pulsed-laser deposition of materials, *Phys. Rev. B*, **48**, pp. 12076–12081.

131. Itina, T. E., Marine, W., and Autric, M. (1997). Monte Carlo simulation of pulsed laser ablation from two-component target into diluted ambient gas, *J. Appl. Phys.*, **92**, pp. 3536–3542.

132. Itina, T. E., Katassonov, A. A., Marine, W., and Autric, M. (1998). Numerical study of the role of a background gas and system geometry in pulsed laser deposition, *J. Appl. Phys.*, **83**, pp. 6050–6054.

133. Geohegan, D. B. (1992). Fast intensified-CCD photography of $YBa_2Cu_3O_{7-x}$ laser ablation in vacuum and ambient oxygen, *Appl. Phys. Lett.*, **60**, pp. 2732–2734.

134. Wood, R. F., Chen, K. R., Leboeuf, J. N., Puretzky, A. A., and Geohegan, D. B. (1997). Dynamics of plume propagation and splitting during pulsed-laser ablation, *Phys. Rev. Lett.*, **79**, pp. 1571–1574.

135. Bailini, A., and Ossi, P. M. (2007). Expansion of an ablation plume in a buffer gas and cluster growth, *Europhys. Lett.*, **79**, p. 35002.

136. Itina, T. E., Hermann, J., Delaporte, P., and Sentis, M. (2002). Laser-generated plasma plume expansion: combined continuous-microscopic modeling, *Phys. Rev. E*, **66**, p. 066406.

137. Sedov, L. I. (1959). *Similarity and Dimensional Methods in Mechanics* (Academic Press, London).

138. Zel'dovich, Y. B. (2002). *Physics of Shock Waves and High-Temperature Hydrodynamic Phenomena* (Courier Corporation).

139. Arnold, N., Gruber, J., and Heitz, J. (1999). Spherical expansion of the vapor plume into ambient gas: an analytical model, *Appl. Phys. A*, **69**, pp. S87–S93.

140. Amoruso, S., Schou, J., and Lunney, J. G. (2010). Energy balance of a laser ablation plume expanding in a background gas, *Appl. Phys. A*, **101**, pp. 209–214.

141. Morel, V., Bultel, A., Annaloro, J., Chambrelan, C., Edouard, G., and Grisolia, C. (2015). Dynamics of a femtosecond/picosecond laser-induced aluminum plasma out of thermodynamic equilibrium in a nitrogen background gas, *Spectrochim. Acta B*, **103–104**, pp. 112–123.

142. Harilal, S. S., Miloshevsky, G. V., Diwakar, P. K., LaHaye, N. L., and Hassanein, A. (2012). Experimental and computational study of complex shockwave dynamics in laser ablation plumes in argon atmosphere, *Phys. Plasmas*, **19**, p. 083504.

143. Chen, Z. Y., and Bogaerts, A. (2005). Laser ablation of Cu and plume expansion into 1 atm ambient gas, *J. Appl. Phys.*, **97**, p. 063305.

144. Song, K. H., and Xu, X. (1998). Explosive phase transformation in excimer laser ablation, *Appl. Surf. Sci.*, **127–129**, pp. 111–116.

145. Yoo, J. H., Jeong, S. H., Greif, R., and Russo, R. E. (2000). Explosive change in crater properties during high power nanosecond laser ablation of silicon, *J. Appl. Phys.*, **88**, pp. 1638–1649.

146. Mafune, F., Kohno, J.-Y., Takeda, Y., and Kondow, T. (2000). Formation of gold nanoparticle by laser ablation in aqueous solution of surfactant, *J. Phys. Chem. B*, **105**, pp. 5114–5120.

147. Compagnini, G., Scalisi, A. A., and Puglisi, O. (2002). Ablation of noble metals in liquids: a method to obtain nanoparticles in a thin polymeric film, *Phys. Chem. Chem. Phys.*, **4**, pp. 2787–2791.

148. Yan, Z., and Chrisey, D. B. (2012). Pulsed laser ablation in liquid for micro-/nanostructure generation, *J. Photochem. Photobiol. C*, **13**, pp. 204–223.

149. Amendola, V., and Meneghetti, M. (2007). Controlled size manipulation of free goldnanoparticles by laser irradiation and their facile bioconjugation, *J. Mater. Chem.*, **17**, pp. 4705–4710.

150. Hashimoto, S., Werner, D., and Uwada, T. (2012). Studies on the interaction of pulsed laserswith plasmonic gold nanoparticles toward light manipulation, heat management, and nanofabrication, *J. Photochem. Photobiol. C*, **13**, pp. 28–54.

151. Besner, S., Kabashin, A. V., Winnik, F. M., and Meunier, M. (2009). Synthesis of size-tunable polymer-protected gold nanoparticle by femtosecond laser-based ablation and seed growth, *J. Phys. Chem. C*, **113**, pp. 9526–9531.

152. Pyatenko, A., Wang, H. Q., Koshizaki, N., and Tsuji, T. (2013). Mechanism of pulse laser interaction with colloidal nanoparticles, *Laser Photonics Rev.*, **7**, pp. 596–604.

153. Wang, H., Pyatenko, A., Kawaguchi, K., Li, X., Swiatkowska-Warkocka, Z., and Koshizaki, N. (2010). Selective pulsed heating for the synthesis of semiconductor and metal submicrometer spheres, *Angew. Chem. Int. Ed*., **49**, pp. 6361–6364.

154. Hess, C., Schwenke, A., Wagener, P., Franzka, S., Sajti, C. L., Pflaum, M., Wiegmann, B., Haverich, A., and Barcikowski, S. (2014). Dose-dependent surface endothelializationand biocompatibility of polyurethane noble metal nanocomposites, *J. Biomed. Mater. Res. A*, **102**, pp. 1909–1920.

155. Kumar, V. L., Siddhardha, R. S. S., Kaniyoor, A., Podila, R., Molli, M., Kumar, S. M. V., Venkataramaniah, K., Ramaprabhu, S., Rao, A. M., and Ramamurthy, S. S. (2014). Gold decoratedgraphene by laser ablation for efficient electrocatalytic oxidation of methanoland ethanol, *Electroanalysis*, **26**, pp. 1850–1857.

156. Zhang, J., Chen, G., Guay, D., Chaker, M., and Ma, D. (2014). Highly active PtAu alloy nanoparticle catalysts for the reduction of 4-nitrophenol, *Nanoscale*, **6**, pp. 2125–2130.

157. Amendola, V., and Meneghetti, M. (2009). Laser ablation synthesis in solution and size manipulation of noble metal nanoparticles, *Phys. Chem. Chem. Phys.*, **11**, pp. 3805–3821.

158. Tamura, A., Sakka, T., Fukami, K., and Ogata, Y. H. (2013). Dynamics of cavitation bubbles generated by multi-pulse laser irradiation of a solid target in water, *Appl. Phys. A*, **112**, pp. 209–213.

159. Ibrahimkutty, S., Wagener, P., Dos Santos Rolo, T., Karpov, D., Menzel, A., Baumbach, T., Barcikowski, S., and Plech, A. (2015). A hierarchical view

on material formation during pulsed-laser synthesis of nanoparticles in liquid, *Sci. Rep*., **5**, p. 16313.

160. Lam, J., Lombard, J., Dujardin, C., Leodoux, G., Merabia, S., and Amans, D. (2016). Dynamical study of bubble expansion following laser ablation in liquids, *Appl. Phys. Lett.*, **108**, p. 074104.
161. Soliman, W., Nakano, T., Takada, N., and Sasaki, K. (2010). Modification of Rayleigh–Plesset theory for reproducing dynamics of cavitation bubbles in liquid-phase laser ablation, *Jpn. J. Appl. Phys.*, **49**, p. 116202.
162. Hilgenfeldt, S., Grossman, S., and Lohse, D. (1999). A simple explanation of light emission in sonoluminescence, *Nature*, **398**, pp. 402–405.
163. Amendola, V., and Meneghetti, M. (2013). What controls the composition and the structure of nanomaterials generated by laser ablation in liquid solution? *Phys. Chem. Chem. Phys.*, **15**, pp. 3027–3046.
164. Dell'Aglio, M., Gaudiuso, R., De Pascale, O., and De Giacomo, A. (2015). Mechanisms and processes of pulsed laser ablation in liquids during nanoparticle production, *Appl. Surf. Sci.*, **348**, pp. 4–9.
165. Ibrahimkutty, S., Wagener, P., Menzel, A., Plech, A., and Barcikowski, S. (2012). Nanoparticle formation in a cavitation bubble after pulsed laser ablation in liquid studied with high time resolution small angle x-ray scattering, *Appl. Phys. Lett.*, **101**, p. 103104.
166. Wagener, P., Ibrahimkutty, S., Menzel, A., Plech, A., and Barcikowski, S. (2013). Dynamics of silver nanoparticle formation and agglomeration inside the cavitation bubble after pulsed laser ablation in liquid, *Phys. Chem. Chem. Phys*., **15**, pp. 3068–3074.
167. Zavedeev, E. V., Petrovskaya, A. V., Simakin, A. V., and Shafeev, G. A. (2006). Formation of nanostructures upon laser ablation of silver in liquids, *Quantum Electron.*, **36**, pp. 978–980.
168. Stratakis, E., Zorba, V., Barberoglou, M., Fotakis, C., and Shafeev, G. A. (2009). Femtosecond laser writing of nanostructure on bulk Al via its ablation in air and liquids, *Appl. Surf. Sci.*, **255**, pp. 5346–5350.
169. Stratakis, E., Zorba, V., Barberoglou, M., Fotakis, C., and Shafeev, G. A. (2009). Laser writing of nanostructures on bulk Al via its ablation in liquids, *Nanotechnology*, **20**, p. 105303.
170. Barmina, E. B., Stratakia, E., Fotakis,C., and Shafeev, G. A. (2010). Generation of nanostructures on metals by laser ablation in liquids: new results, *Quantum Electron.*, **40**, pp. 1012–1020.
171. Podagatlapalli, G. K., Hamad, S., Sreedhar, S., Tewari, S. P., and Rao, S. V. (2012). Fabrication and characterization of aluminum nanostructures

and nanoparticles obtained using femtosecond ablation technique, *Chem. Phys. Lett.*, **530**, pp. 93–97.

172. Fan, P., Zhong, M., Li, L., Schmitz, P., Lin, C., Long, J., and Zhang, H. (2014). Angle-independent colorization of copper surfaces by simultaneous generation of picosecond-laser-induced nanostructures and redeposited nanoparticles, *J. Appl. Phys.*, **115**, p. 124302.